4 Electrical resistivity method

In this chapter the electrical resistivity method, a mainstay of near-surface applied geophysics for many decades (Keller and Frischknecht, 1966; Bhattacharya and Patra, 1968) is described. The technique has enjoyed a resurgence in popularity since the mid 1990s (Loke, 2000; Dahlin, 2001; Zonge *et al*., 2005) due to rapid and impressive advancements in data acquisition, forward modeling, and inversion capabilities.

The fundamental steps involved in the resistivity method may be outlined as follows. An electric current I [amperes, A] is directly injected into the ground through a pair of electrodes and the resulting voltage V [volts, V] is measured between a second pair of electrodes. The impedance $Z = V/I$ [V/A] of the Earth is formed; it is the ratio of the voltage output V measured at the potential electrodes to the current input I at the current electrodes. The impedance is then transformed into an apparent resistivity ρ_a [ohm-meters, Ωm] which is an intuitively understood indicator of the actual underlying electrical resistivity structure $\rho(\mathbf{r})$ of the Earth, where $\mathbf{r}$ is the position vector. Different arrangements of the electrodes permit the apparent resistivity to be determined at different depths and lateral positions. A map of the apparent resistivity plotted at these locations is termed a *pseudosection* (Loke, 2000). The pseudosection is then inverted to obtain a two- or three-dimensional (2-D or 3-D) resistivity section $\rho(\mathbf{r})$ of the ground. Finally, a geological interpretation of the resistivity section is performed that incorporates, as far as possible, any prior knowledge based on outcrops, supporting geophysical or borehole data, and any information gained from laboratory studies of the electrical resistivity of geological materials (see Table 4.1).

Table 4.1 Resistivity of common geological materials

Geomaterial	Resistivity [Ωm]
Clay	1–20
Sand, wet to moist	20–200
Shale	1–500
Porous limestone	100–10^3
Dense limestone	10^3–10^6
Metamorphic rocks	50–10^6
Igneous rocks	10^2–10^6

4.1 Introduction

The electrical resistivity method has a long history in applied geophysics, including the pioneering work in 1912 by Conrad Schlumberger of France. A few years earlier than that, Swedish explorationists had experimented with locating conductive bodies by moving around a first pair of potential electrodes while keeping a second pair of current electrodes in a fixed location (Dahlin, 2001).

The two case histories described below introduce the reader to examples of recent usage of the resistivity method. The first example is a study of a hydrogeological problem at a human-impacted site of historical significance. The second example relates to the use of resistivity data for imaging liquid hazardous waste at a nuclear-waste site in the USA.

Example. Investigation of an historic WWII site.

The D-Day invasion site at Pointe du Hoc, France (Figure 4.1a) is an important WWII battlefield and remains today a valuable cultural resource but its existence is jeopardized by the risk of potentially devastating cliff collapses. The resistivity method was used there to study the effect of groundwater infiltration on the cliff stability. The great amount of buried steel, concrete, and void spaces at the site renders hydrogeological interpretation of the resistivity data challenging.

A resistivity profile was acquired by laying out a line of electrodes passing within a few meters of a 155-mm gun casemate (Figure 4.1b). The resistivity section shown in

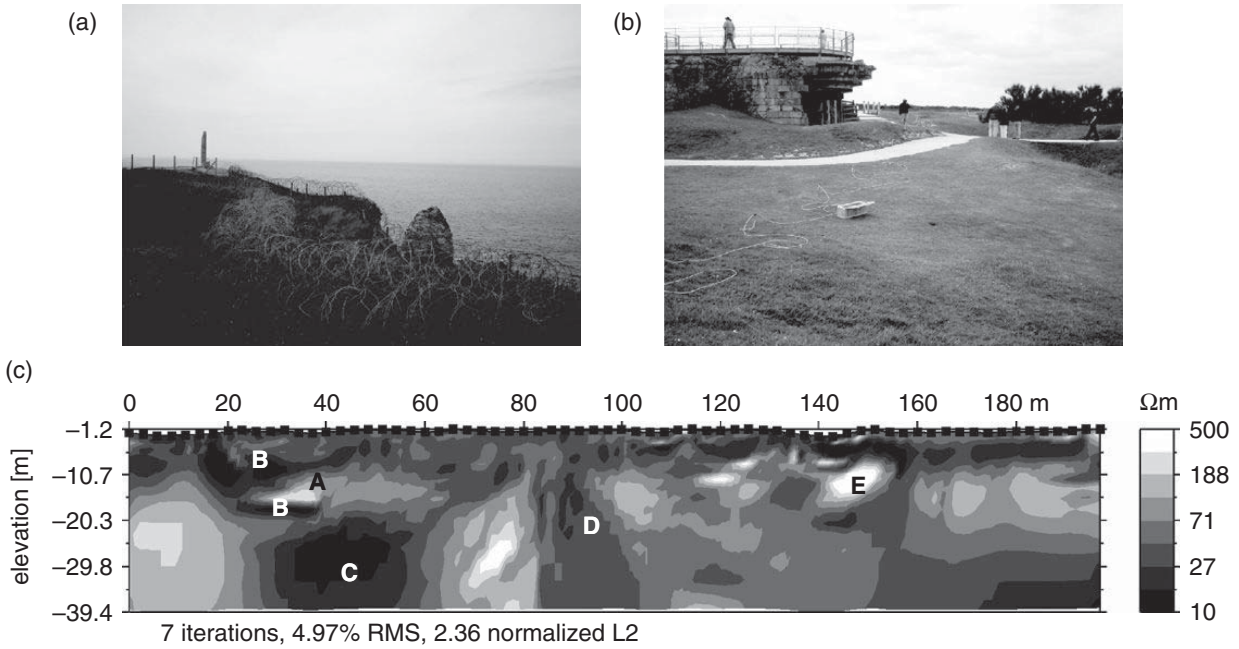

Figure 4.1 (a) WWII battlefield, Pointe du Hoc, France. (b) Resistivity data acquisition passing close to an historic German fortification. (c) Resistivity section showing natural and cultural subsurface features. Labels A–E described in the text. After Everett *et al*. (2006).

Figure 4.1c was constructed and interpreted by Everett *et al*. (2006), as follows. The small zone of high resistivity (A) showing at ~ 15 m depth, with the low-resistivity halo (B) surrounding it, is the geophysical signature of the casemate and its foundations. The larger, deeper low-resistivity zone (C) extending from 25 to 60 m along the profile is likely of geological origin, perhaps a zone of groundwater accumulation. The vertical zone of high conductivity (D) at ~ 90 m is not immediately associated with any known cultural features; it is interpreted as a vertical conduit for groundwater that flows from substantial depths to the surface. The highly resistive zone (E) at distance 145–150 m along the profile is explained by a large slab of buried concrete.

Example. Investigation of the Hanford nuclear site.

Discharge of millions of liters of hazardous liquid electrolytes since the 1940s has occurred at the Hanford nuclear facility in eastern Washington State, USA. Subsurface resistivity imaging of the resulting contaminant plumes in the vadose zone beneath the site remains a challenging task due to the presence of storage tanks, pipelines, metal fences, and other cultural infrastructure. To directly access the deep vadose region beneath the near-surface zone of cultural noise, Rucker *et al*. (2010) took advantage of the large number of existing steel-cased monitoring wells at the site. They utilized the steel casings as long cylindrical electrodes in a novel well-to-well (WTW) pole–pole configuration.

A total of 110 steel casings from wells with lengths up to 90 m were used as electrodes in the WTW survey. The resulting voltage measurements were of reasonable quality, with only ~ 10% of the ~ 12 000 readings being rejected due to high repeat errors. The result of a 3-D inversion of data from 87 centrally located wells is shown in Figure 4.2. Two major low-resistivity anomalies can be identified in this plan-view map at depth 1.4 m. The first, in the lower-left region of the survey, corresponds to the area of a historical non-point source dispersal of nitrate-contaminated (1–2 mol/L) wastewater. The second low-resistivity anomaly occurs in the vicinity of leaking storage tanks T-103 and T-106. The tanks are documented to have discharged into the vadose zone a volume of liquid contaminant exceeding 440 kL.

4.2 Fundamentals

The resistivity technique is founded on basic principles familiar to all scientists and engineers working in the physical sciences. Consider a cylindrical sample of material of length L [m], resistance R [Ω] and cross-sectional area A [m^2]. The resistivity ρ [Ωm] is a material property equal to $\rho = RA/L$, see Figure 4.3. The spatially variable resistivity

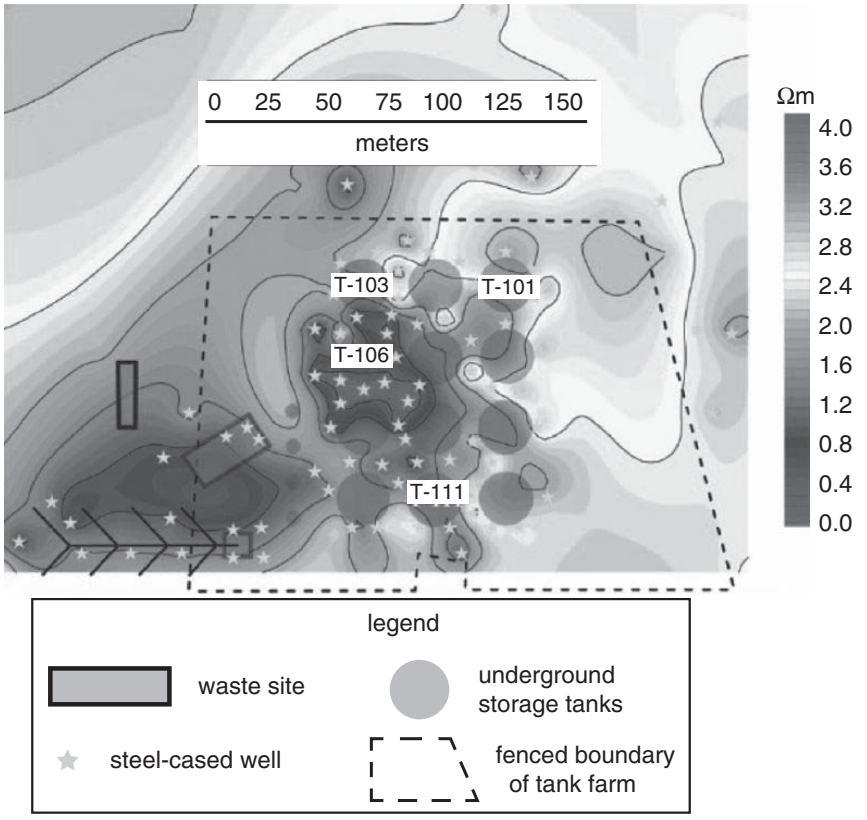

Figure 4.2 WTW resistivity inversion at the Hanford nuclear facility; depth slice at 1.4 m. After *Rucker et al*. (2010).

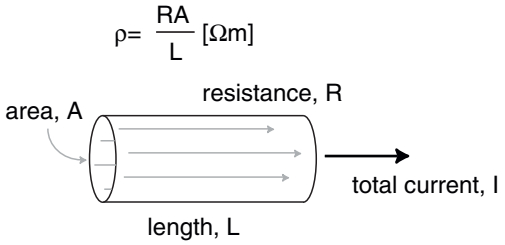

Figure 4.3 Definition of resistivity ρ.

$\rho(\mathbf{r})$ of the subsurface is the physical property that is sensed by the resistivity method. The reciprocal of the resistivity is the electrical conductivity $\sigma = 1/\rho$, which by convention is the preferred quantity used in the electromagnetic and ground-penetrating radar geophysical techniques (see Chapters 8 and 9). Electrical conductivity is a measure of the ability of a material to sustain long-term electric current flow. Thus, electric current can flow readily in low-resistivity zones and is weak or absent in high-resistivity zones.

A general scenario is shown in Figure 4.4, in which a battery is connected to two electrodes which serve as a current source/sink pair. The electric current streamlines (line segments) and equipotentials (colors) are displayed in the figure for a current injection of $I = 1$ A and uniform resistivity $\rho = 1$ Ωm.

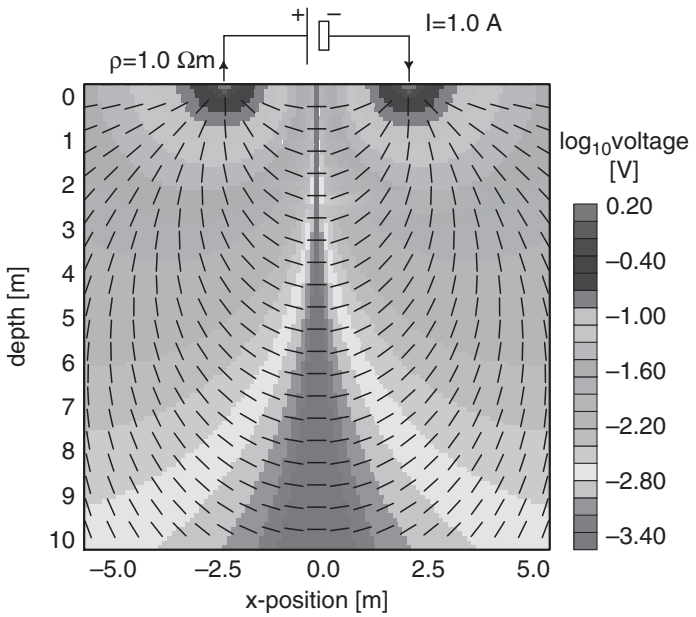

Figure 4.4 Potential and streamlines of electric current for a point source and a point sink of current.

To understand how the resistivity method is used to estimate Earth resistivity, first recognize that the subsurface current density $\mathbf{J}$ is related to the electric field $\mathbf{E}$ by Ohm's law $\mathbf{J} = \sigma\mathbf{E}$ so that

$$\mathbf{E} = \frac{\mathbf{J}}{\sigma} = \rho\mathbf{J} = \frac{I\rho\,\hat{\mathbf{r}}}{4\pi r^2}. \tag{4.1}$$

Ohm's law, stated in Equation (4.1), is nothing more than the generalization to continuous media of the familiar law as it applies to a simple resistive circuit, $V = IR$, where V is voltage, I is current, and R is resistance.

Next, consider an electric current I injected, at the origin of a spherical coordinate system, into a hypothetical whole-space of uniform resistivity ρ. Suppose the return electrode is placed at infinity. The situation is depicted in Figure 4.5. In the vicinity of the injection point, the current will spread out symmetrically in all three dimensions. At point P at distance r from the injection point, using Equation (4.1) the current density $\mathbf{J}$ is

$$\mathbf{J} = \frac{I\,\hat{\mathbf{r}}}{4\pi r^2}, \tag{4.2}$$

where $4\pi r^2$ is the area of a spherical surface of radius r. The numerator of Equation (4.2) expresses the magnitude and direction of the current at point P while the denominator expresses the cross-sectional area through which the current uniformly flows.

What is the voltage V measured at observation point P in Figure 4.5? Voltage is *defined* as the work done by the electric field $\mathbf{E}$ in moving a test charge from infinity to point P. Work is defined by the product of work and distance, or in our case the line integral

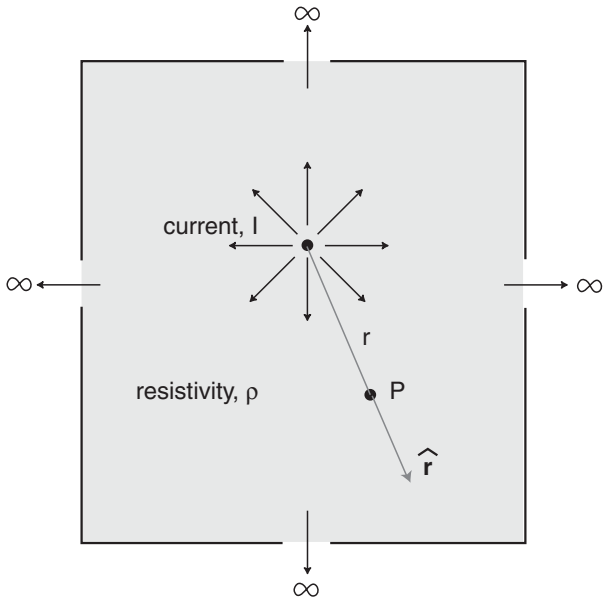

Figure 4.5 Current injection into a wholespace of uniform resistivity ρ.

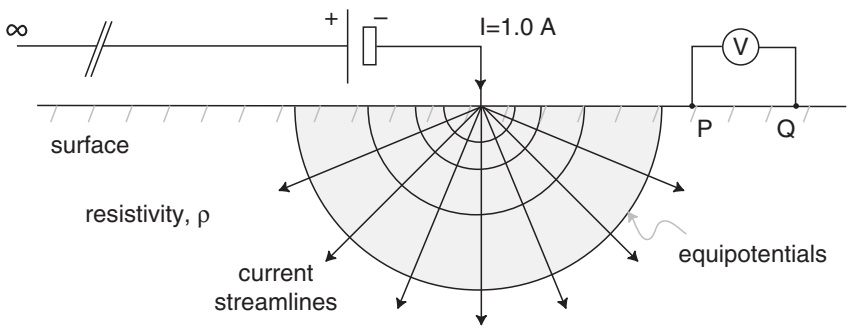

Figure 4.6 Voltage measured between points *P* and *Q* for a point source of electric current injected into a halfspace of uniform resistivity ρ.

$$V = \int_C \mathbf{E} \cdot d\mathbf{s}, \tag{4.3}$$

where C is any path from infinity terminating at point P. Hence the voltage at P is

$$V = \int_r^\infty \mathbf{E} \cdot d\mathbf{r} = \int_r^\infty \frac{I\rho}{4\pi r^2} dr = \frac{I\rho}{4\pi r}. \tag{4.4}$$

Now suppose that the injection point is located on the surface of a halfspace representing the Earth, as shown in Figure 4.6.

The electric current, which cannot flow through the non-conducting air, flows radially outward through a *hemisphere* of radius r and surface area $2\pi r^2$. Hence, the current density

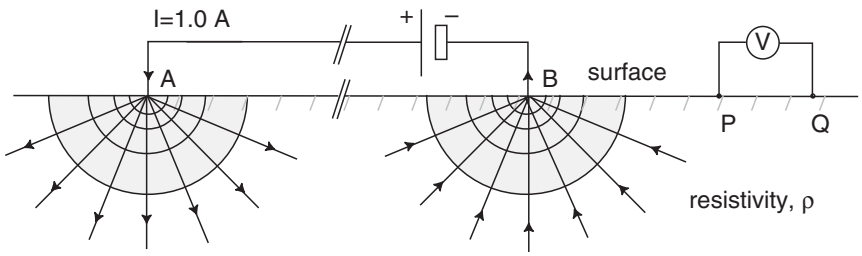

Figure 4.7 Voltage measured between points *P* and *Q* for a point source *A* and point sink *B* of electric current.

in this case is $\mathbf{J} = I\hat{\mathbf{r}}/2\pi r^2$ so that, using Equations (4.1) and (4.4), the voltage measured at point P is $V = I\rho/2\pi r_P$ where r_P is the distance from the current source to the potential electrode P. This is the basic equation of resistivity. The voltage measured across the terminals P and Q of the voltmeter is the difference

$$V_{PQ} = V_P - V_Q = \frac{I\rho}{2\pi}\left[\frac{1}{r_P} - \frac{1}{r_Q}\right], \tag{4.5}$$

where r_Q is the distance from the current source to the potential electrode Q.

Apparent resistivity. Equation (4.5) is derived under the assumption that the Earth has a uniform resistivity ρ. In reality, the resistivity distribution inside the Earth is heterogeneous. We can re-arrange Equation (4.5) to solve for an *apparent resistivity* ρ_a

$$\rho_a = \frac{2\pi V_{PQ}}{I}\left[\frac{1}{r_P} - \frac{1}{r_Q}\right]^{-1} = \kappa Z, \tag{4.6}$$

which is interpreted to be the resistivity that would have been measured if the Earth were in fact homogeneous. Notice that the apparent resistivity can be written as a product of the measured Earth impedance $Z = V/I$ and a *geometric factor* κ that depends only on the arrangement of the current and potential electrodes. In the configuration shown in Figure 4.6, which is known as a *pole–dipole* arrangement, the geometric factor is simply

$$\kappa = 2\pi\left[\frac{1}{r_P} - \frac{1}{r_Q}\right]^{-1}. \tag{4.7}$$

Although the pole–dipole arrangement has received attention from near-surface geophysicists, a more general exploration scenario is the arbitrary four-electrode configuration shown in Figure 4.7 which includes a point source and the return point sink of current. The geometric factor is $\kappa = 2\pi/[1/r_{AP} - 1/r_{AQ} - 1/r_{BP} + 1/r_{BQ}]$.

Four-electrode arrays. Historically, a number of four-electrode configurations have proven popular for a wide range of applications of geophysics. As we describe below, computer-controlled configurations of hundreds of electrodes are now in routine use (Loke, 2000). Nevertheless it remains worthwhile to briefly discuss a few of the traditional four-electrode configurations (Figure 4.8) in order to gain insight into the capabilities of the resistivity method and to explore the advantages and disadvantages of the various electrode configurations in terms of depth penetration, lateral resolution, ease of deployment, and

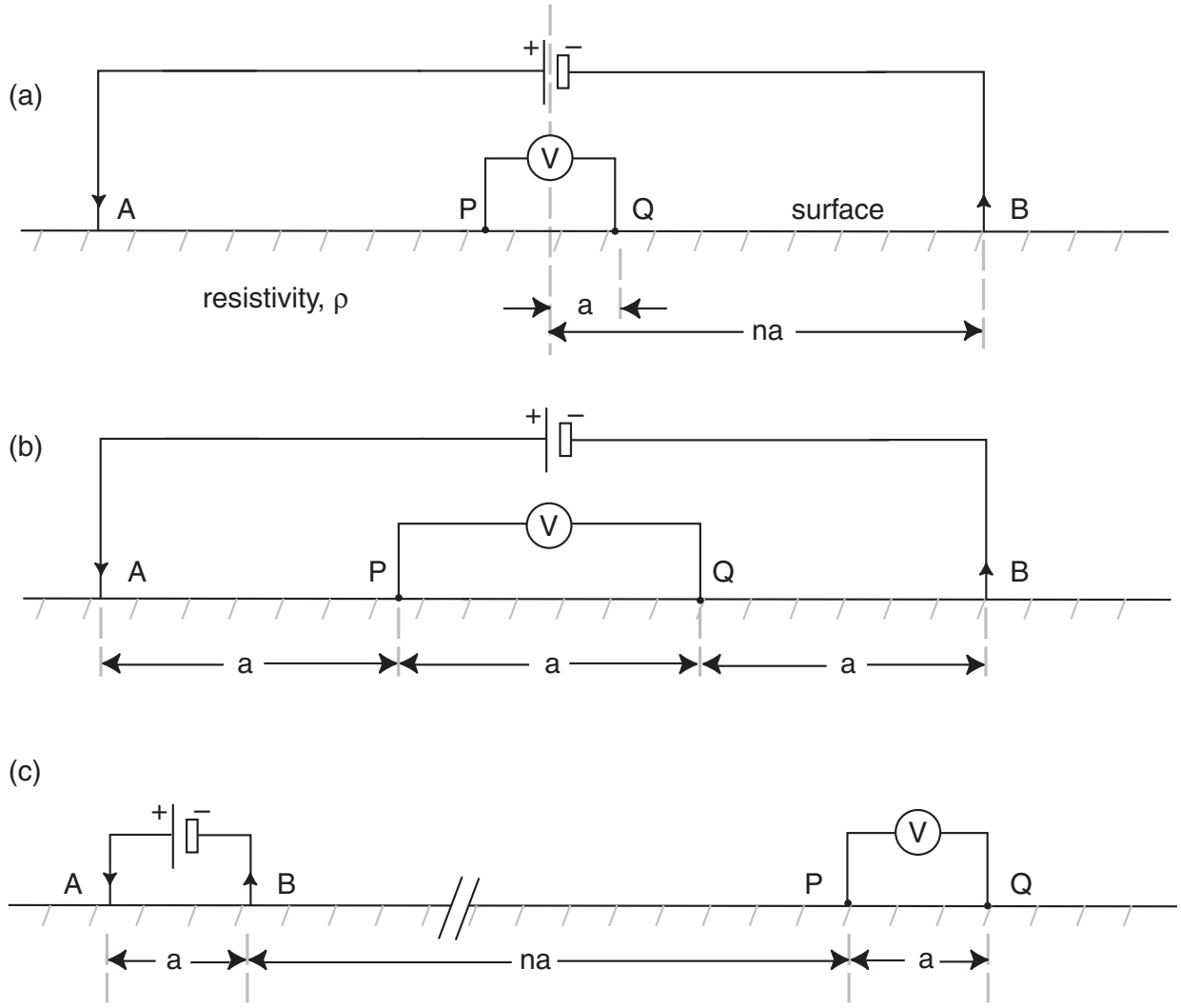

Figure 4.8 Traditional four-electrode configurations: (a) Schlumberger; (b) Wenner; (c) dipole–dipole.

signal-to-noise ratio. A review of these and many other popular electrode configurations is given in Zonge *et al*. (2005).

The Schlumberger array (Figure 4.8a) is designed for *sounding*, that is, determining the Earth resistivity depth profile $\rho(z)$ beneath a single location. The potential electrodes PQ are kept centered at a fixed location with constant separation $2a$. The current electrodes AB are centered at the same location but voltage readings are made as the separation between them is expanded about the common midpoint. In this way, apparent resistivity is determined as a function of the current-electrode separation. It is traditional to display Schlumberger array data as a graph of the form $\rho_a(AB/2)$, where $AB/2$ is one-half of the current-electrode separation. The geometric factor for the Schlumberger array is,

$$\text{Schlumberger} : \kappa = (n-1)(n+1)\pi a/2. \tag{4.8}$$

A Schlumberger sounding can achieve excellent depth penetration with sufficiently large AB separations. The array has limited lateral resolution however, as it is designed for

vertical sounding. The Schlumberger array is cumbersome in the field since its traditional deployment requires lengthy wire connections that must be re-positioned for each measurement. The signal-to-noise ratio is moderate to good. The voltage reading is taken in the middle of the array which suggests that a good signal level should be achieved. However, as shown in Figure 4.4, voltages are generally low at the midpoint between the injection and withdrawal electrodes (the warm colors indicate low voltages), at least over a uniformly resistive Earth.

The Wenner array (Figure 4.8b) is designed for lateral profiling to determine the Earth resistivity $\rho(x)$ at a roughly constant depth of penetration. There is a fixed separation of a between adjacent electrodes, with the potential electrodes PQ placed inside the current electrodes AB as in the Schlumberger array. Apparent resistivity is determined as the array is moved along a lateral profile. It is easy to see that the geometric factor for the Wenner array is

$$\text{Wenner: } \kappa = 2\pi a. \tag{4.9}$$

The penetration depth of the Wenner array depends on the spacing a; the larger its value, the deeper the penetration. In simple terms, as the spacing between the injection and withdrawal electrodes increases, electric current is driven deeper into the subsurface. The Wenner array is quite effective at mapping lateral contrasts in resistivity within the depth of penetration. The array is moderately easy to deploy as the trailing electrode can be leapfrogged to the front as the configuration is advanced along the profile. This means that only one electrode movement is required per measurement. Signal-to-noise ratio is generally good since the potential electrodes PQ are located in the central part of the array and, unlike those in the Schlumberger array, are relatively widely spaced for a given current-electrode separation AB.

The dipole–dipole configuation is shown in Figure 4.8c. The current electrodes AB and the potential electrodes PQ have the same spacing a but the two pairs are widely separated by a distance na, where $n >> 1$. The geometric factor for the dipole–dipole array is

$$\text{dipole}-\text{dipole: } \kappa = \pi n(n+1)(n+2)a. \tag{4.10}$$

The dipole–dipole array offers advantages of both Schlumberger depth sounding and Wenner lateral profiling. However, the signal-to-noise ratio deteriorates at large values of n and the voltage measurements across the electrodes PQ are susceptible to distortion by small-scale, near-surface heterogeneities.

4.3 Sensitivity functions

Measurements made using the resistivity technique are sensitive to spatial averages of the near-surface electrical resistivity distribution. The details of the averaging process depends on the type of array used. Furman *et al*. (2003) have examined the spatial sensitivity of standard four-electrode arrays, plus that of a non-standard, partially overlapping array. A sensitivity function S is defined as the magnitude of the perturbation in the voltage

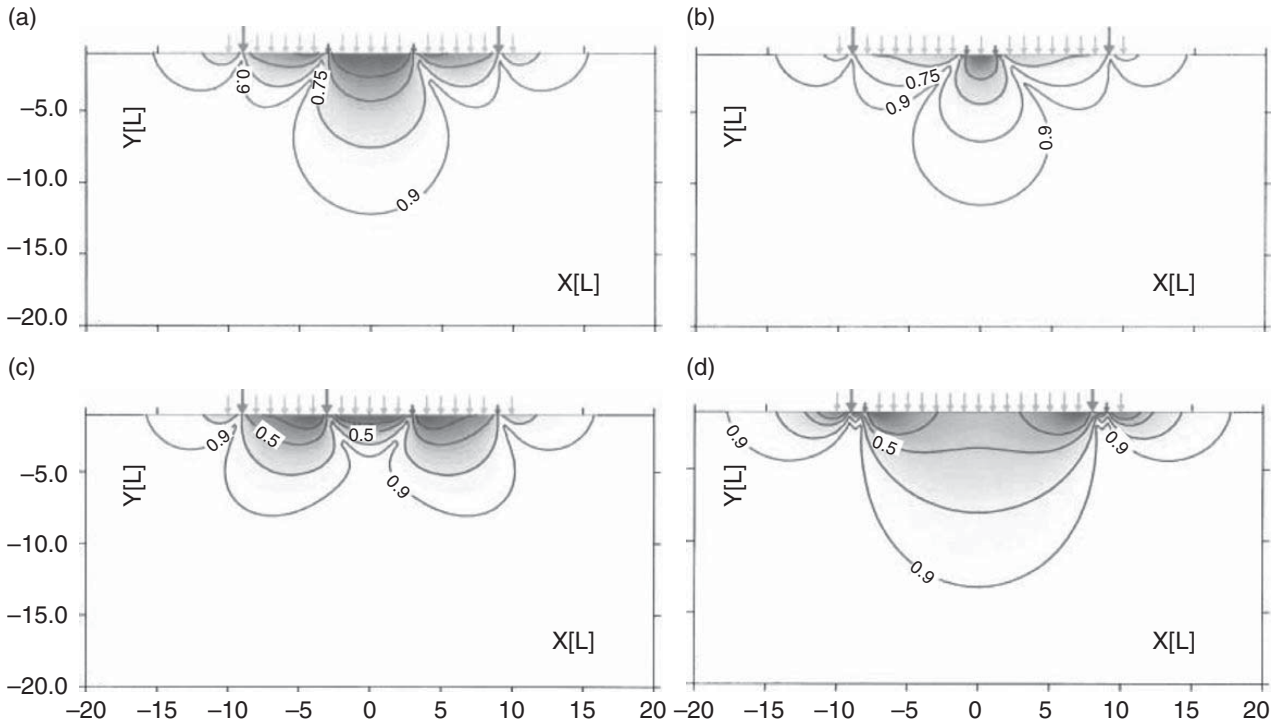

Figure 4.9 Sensitivity functions for four-electrode arrays: (a) Wenner; (b) Schlumberger; (c) dipole–dipole; (d) partially overlapping. Larger, bold arrows show current injection and withdrawal points; Smaller, bold arrows show potential measurement points. After Furman *et al*. (2003).

measurement due to a small perturbation in the subsurface resistivity distribution. For this purpose, Furman *et al*. (2003) use a 2-D analytic solution for a small buried cylindrical heterogeneity of radius L and they slightly perturb the resistivity of the cylinder. The cumulative sensitivity function $CS(x, y)$ corresponds to the summation of the sensitivities due to perturbations in voltage measurements caused as the cylindrical heterogeneity is placed at a number of locations in the subsurface.

Plotted in Figure 4.9 is the cumulative sensitivity function $CS(x, y)$ for the four array types analyzed by Furman *et al*. (2003). The plots show contours of $CS(x, y)$ at the 25, 50, 75 and 90% levels. The intepretation of the 90% level, for example, is that 10% of the measurement sensitivity of the array lies outside the 90% contour. In other words, these plots give a good indication of the region of the subsurface to which a given measurement array is sensitive. The Wenner array (Figure 4.9a), for example, is sensitive to the ground mainly beneath the center of the array but has moderate sensitivity across the entire array, which confirms its utility as a lateral profiling configuration. In Figure 4.9b it can be seen that the Schlumberger array, as expected for a vertical sounding configuration, is most sensitive to the near-surface immediately below the potential electrodes and less sensitive elsewhere. As shown in Figure 4.9c, the dipole–dipole array is most sensitive to the regions immediately beneath the current and potential electrodes, with less sensitivity to the intervening region between the two dipoles. The area enclosed by the 90% contour is small, as expected, since it is well known that the dipole–dipole array generally has poor signal-to-noise ratio and high sensitivity to near-surface heterogeneities. As shown by the large size of the 90% contour

in Figure 4.9d, the non-standard partially overlapping configuration offers uniformly high sensitivity across a wide and deep region beneath the entire array.

4.4 Multi-layer models

The above discussion outlined the formulas necessary to compute voltages that would be recorded over a homogeneous Earth. In the case of multiple layers of uniform resistivity, the calculations are more involved. Generally, the electric potential $\varphi(\mathbf{r})$ inside the Earth obeys the differential equation

$$\nabla\cdot(\sigma\nabla\varphi) = 0; \tag{4.11}$$

where $\sigma(\mathbf{r}) = 1/\rho(\mathbf{r})$ is the spatially variable electrical conductivity. Within each uniform layer of an N-layered medium, Equation (4.11) reduces to the Laplace equation $\nabla^2\varphi = 0$. For point-source excitation, we can use 2-D cylindrical coordinates (r, z) with azimuthal symmetry. The general solution to the Laplace equation in that case is (Bhattacharya and Patra, 1968)

$$\varphi(r,z) = \int_0^\infty [A(\lambda)\exp(-\lambda z) + B(\lambda)\exp(+\lambda z)]J_0(\lambda r)d\lambda. \tag{4.12}$$

where $J_0(\lambda r)$ is the zeroth-order Bessel function. A special case occurs for a uniform halfspace of resistivity ρ; the primary potential φ_P due to a single point of current I injected at the origin $(r, z) = (0,0)$ is

$$\varphi_P(r,z) = \frac{I\rho}{2\pi}\int_0^\infty \exp(-\lambda z)J_0(\lambda r)d\lambda. \tag{4.13}$$

Using the Bessel function identity

$$\frac{1}{R} = \int_0^\infty \exp(-\lambda z)J_0(\lambda r)d\lambda, \tag{4.14}$$

the primary potential reduces to the expression that we derived earlier, namely,

$$\varphi_P(r,z) = \frac{I\rho}{2\pi R}, \tag{4.15}$$

with $R = \sqrt{r^2 + z^2}$.

The formula for the apparent resistivity ρ_a over a two-layer Earth ($N = 2$) is obtained by writing the general solution for $\varphi(r, z)$ in each uniform layer and then matching fundamental boundary conditions at the layer interfaces. The solutions in the first and second layers are, respectively,

$$\varphi_1(r,z) = \frac{I\rho_1}{2\pi R} + \int_0^\infty [A_1(\lambda)\exp(-\lambda z) + B_1(\lambda)\exp(+\lambda z)]J_0(\lambda r)d\lambda; \tag{4.16}$$

$$\varphi_2(r,z) = \frac{I\rho_1}{2\pi R} + \int_0^\infty A_2(\lambda)\exp(-\lambda z)J_0(\lambda r)d\lambda; \tag{4.17}$$

which have the form of a sum of the primary $\varphi_P = I\rho_1/2\pi rR$ and a secondary potential. Notice that Equation (4.17) does not include a term of the form $\exp(+\lambda z)$ since the potential should vanish at great distance from the source, $z \to +\infty$. The boundary conditions are the continuity of normal electric current at $z = 0$ and the continuity of tangential electric field and normal current at the layer interface, $z = h_1$. These conditions are

$$\frac{\partial\varphi_1}{\partial z}\Big|_{z=0} = 0; \tag{4.18}$$

$$\varphi_1\big|_{z=h_1} = \varphi_2\big|_{z=h_1}; \tag{4.19}$$

$$\frac{1}{\rho_1}\frac{\partial\varphi_1}{\partial z}\Big|_{z=h_1} = \frac{1}{\rho_2}\frac{\partial\varphi_2}{\partial z}\Big|_{z=h_1}. \tag{4.20}$$

The three boundary conditions (4.18–4.20) are sufficient to determine the unknown coefficients (A_1, B_1, A_2). Applying the boundary conditions results in the solution at the surface $z = 0$,

$$\varphi(r) = \frac{I\rho_1}{2\pi}\int_0^\infty k_{12}(\lambda)J_0(\lambda r)d\lambda \tag{4.21}$$

where

$$k_{12}(\lambda) = \frac{1 - u_{12}\exp(-2\lambda h_1)}{1 + u_{12}\exp(-2\lambda h_1)} \tag{4.22}$$

and

$$u_{12} = \frac{\rho_1 - \rho_2}{\rho_1 + \rho_2} \tag{4.23}$$

is interpreted as a reflection coefficient.

Electric-current streamlines for two cases, a resistive layer over a conducting halfspace, and a conducting layer over a resistive halfspace, are shown in Figure 4.10. It is readily observed that the electric current patterns in the underlying medium 2 are similar for both cases. In the overlying medium 1, the horizontal electric current flow is better developed in the conductive case (Figure 4.10b) than in the resistive case (Figure 4.10a). This accords with the definition of electrical conductivity as a material property that measures its capability to sustain long-term, or steady-state, electric-current flow.

For the four-electrode Schlumberger configuration deployed over a two-layer Earth, the apparent resistivity formula is the sum of terms like (4.21), namely,

$$\rho_a = \frac{I\rho_1}{2\pi}\int_0^\infty k_{12}(\lambda)[J_0(\lambda r_1) - J_0(\lambda r_2) - J_0(\lambda r_3) + J_0(\lambda r_4)]d\lambda. \tag{4.24}$$

Generalizing this procedure to the case of $N = 3$ layers, the reader should be able to derive the corresponding formula

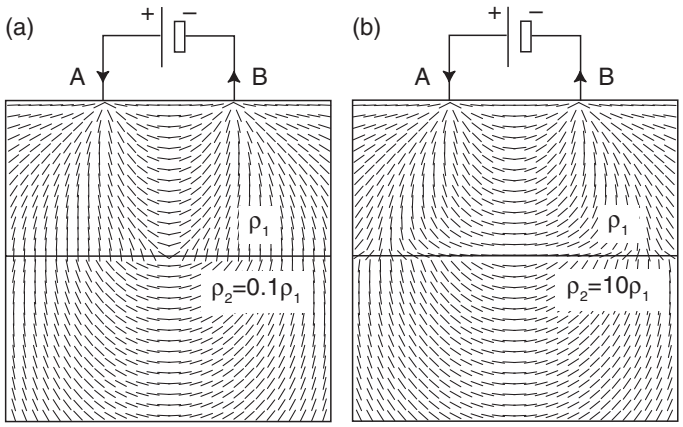

Figure 4.10 Electric-current streamlines for current source and sink over a two-layer Earth: (a) resistor-over-conductor; (b) conductor-over-resistor.

$$\rho_a = \frac{I\rho_1}{2\pi}\int_0^\infty k_{123}(\lambda)[J_0(\lambda r_1) - J_0(\lambda r_2) - J_0(\lambda r_3) + J_0(\lambda r_4)]d\lambda \tag{4.25}$$

where

$$k_{123}(\lambda) = \frac{1 - u_{123}\exp(-2\lambda h_1)}{1 + u_{123}\exp(-2\lambda h_1)} \tag{4.26}$$

$$u_{123} = \frac{\rho_1 - \rho_2 k_{23}}{\rho_1 + \rho_2 k_{23}} \tag{4.27}$$

$$k_{23}(\lambda) = \frac{1 - u_{23}\exp(-2\lambda h_2)}{1 + u_{23}\exp(-2\lambda h_2)} \tag{4.28}$$

$$u_{23} = \frac{\rho_2 - \rho_3}{\rho_2 + \rho_3}. \tag{4.29}$$

Further generalization of the formula (4.25) to an arbitrary number of layers should be obvious.

Schlumberger sounding curves $\rho_a(AB/2)$ for three-layer Earth models are shown in Figure 4.11, for the different classes of resistivity models shown in Table 4.2. The sounding curves are obtained by solving Equation (4.25), for each type of resistivity model, with AB the distance between the current electrodes. Notice that the sounding curves resemble smoothed versions of the actual resistivity structure, which facilitates their qualitative geological interpretation.

The formulas for apparent resistivity over a layered Earth, such as (4.24) or (4.25), requires the evaluation of Hankel transforms of the form

$$f(r) = \int_0^\infty K(\lambda)J_0(\lambda r)d\lambda. \tag{4.30}$$

A Hankel transform can be regarded as a type of *digital filter* which takes a known kernel function $K(\lambda)$ and converts it into a function $f(r)$ that is to be determined. Following the

Table 4.2 Classes of three-layer Schlumberger sounding curves, after Bhattacharya and Patra (1968)

Model type	Resistivity values
H (minimum)	$\rho_1 > \rho_2 < \rho_3$
Q (double descending)	$\rho_1 > \rho_2 > \rho_3$
A (double ascending)	$\rho_1 < \rho_2 < \rho_3$
K (maximum)	$\rho_1 < \rho_2 > \rho_3$

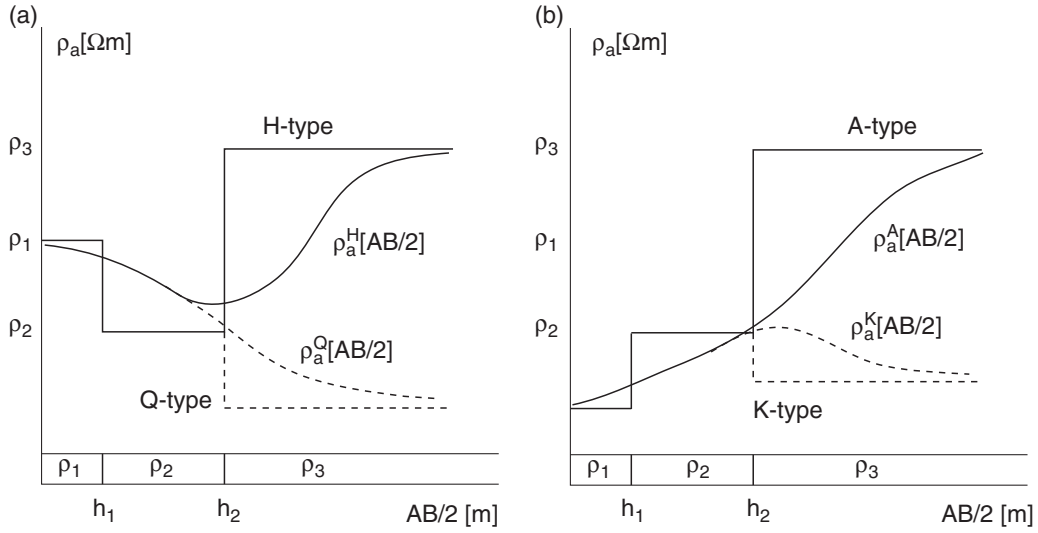

Figure 4.11 Schlumberger three-layer apparent-resistivity sounding curves: (a) H-type and Q-type models; (b) A-type and K-type models (see text for details). After Bhattacharya and Patra (1968)

approach of Guptasarma and Singh (1997), the unknown function $f(r)$ is written as a linear combination of filter weights W_i, $i = 1, \ldots, N$, that is,

$$f(r) = \frac{1}{r} \sum_{i=0}^{N} W_i K(\lambda_i) \tag{4.31}$$

where the kernel is sampled at the logarithmically spaced points

$$\lambda_i = \frac{1}{r} 10^{a+(i-1)s}. \tag{4.32}$$

The J_0-transform in Equation (4.30) can be solved using the weights found by Guptasarma and Singh (1997), for filter lengths of $n = 61$ and $n = 120$. The digital filter can then be checked against several analytic cases, such as

$$\int_0^\infty \exp(-c\lambda) J_0(\lambda r) \mathrm{d}\lambda = \frac{1}{c^2 + r^2} \tag{4.33}$$

$$\int_0^\infty \lambda \exp(-c\lambda^2) J_0(\lambda r) \mathrm{d}\lambda = \frac{1}{2c} \exp\left(-\frac{r^2}{4c}\right) \tag{4.34}$$

$$\int_0^\infty \lambda \exp(-c\lambda) J_0(\lambda r) \mathrm{d}\lambda = \frac{c}{(c^2 + r^2)^{3/2}} \tag{4.35}$$

The filter weights W_i and the two parameters (a, s) in Equation (4.32) were found by Guptasarma and Singh (1997) based on a least-squares fit to the particular transform given by Equation (4.35). There are a large number of other numerical techniques for evaluating Hankel transforms that can be found in the literature, some of these are listed in Chapter 8.

4.5 Azimuthal resistivity

Many applications of near-surface geophysics require an understanding of the hydrogeological behavior of fractured geological formations. Fluid flow in fractured systems is important for studies of safe waste disposal, contaminant transport, and groundwater discovery and management. Fracturing of a low-permeability rock formation can dramatically enhance the hydraulic conductivity. Bulk properties of a fractured aquifer, such as fracture distribution, aperture distribution, effective porosity, and permeability, are difficult to obtain directly. However, these important parameters may be measured indirectly using the *azimuthal resistivity* method.

A fractured, or jointed, rock formation is inherently *anisotropic* if the fractures are preferentially aligned along one or more certain directions. Consider a vertically jointed rock formation, an idealization of which is shown in Figure 4.12 (top right). The along-strike direction in this case is assumed to be in the y-direction, as indicated by the coordinate axes. Similarly, across-strike is x-directed. Other classes of anisotropy are

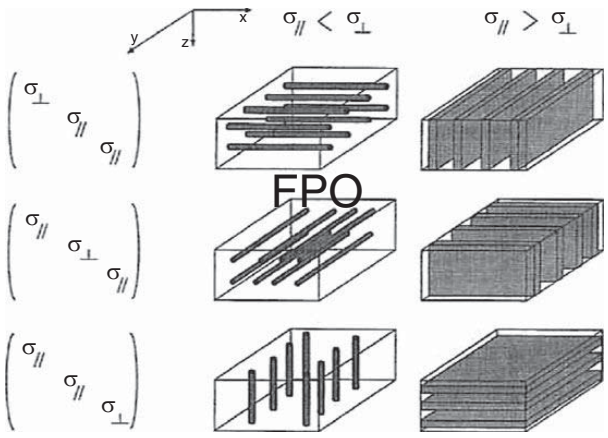

Figure 4.12 Representation of an anisotropic medium by conducting rods and sheets. After Everett and Constable (1999).

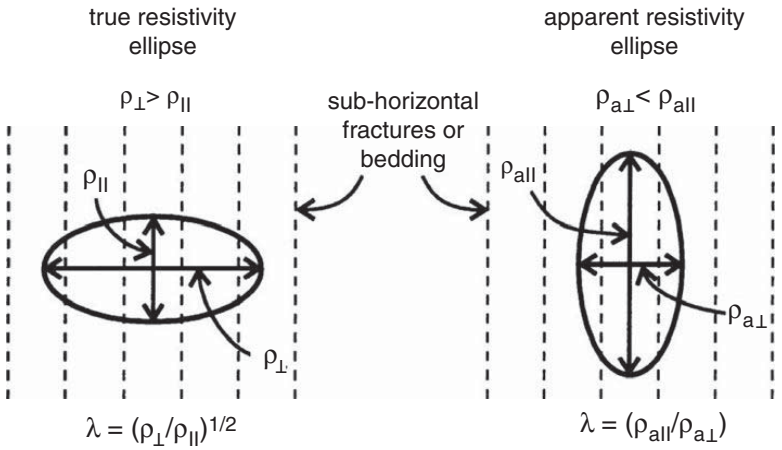

Figure 4.13 True and apparent resistivity ellipses, based on the Wenner linear electrode array, showing the paradox of anisotropy. The coefficient of anisotropy is λ. After Watson and Barker (1999).

shown in the remaining panels of Figure 4.12. The *uniaxial* conductivity tensor σ is also shown with its principal axes aligned along-strike and across-strike relative to the anisotropic geological structure. Notice that the electrical conductivity of an anisotropic rock formation, by definition, depends on the direction in which it is measured.

The apparent resistivity for the Wenner array aligned at angle θ with respect to the strike of the anisotropy of a vertically fractured medium is given by Bhattacharya and Patra (1968) as

$$\rho_a(\theta) = \sqrt{\frac{\rho_\perp \rho_{||}}{\cos^2\theta + (\rho_\perp \rho_{||})\sin^2\theta}}. \tag{4.36}$$

Note that for $\theta = 0$, the Wenner array is aligned with the fractures along the strike of the anisotropy, but according to the previous equation we find $\rho_a(0) = \sqrt{\rho_\perp \rho_{||}}$, not $\rho_{||}$ as would be expected. Similarly, when the array is aligned across the strike of the fractures such that $\theta = \pi/2$ we find $\rho_a(\pi) = \rho_{||}$, not $\rho\perp$ as expected. These two results are collectively termed the *paradox of anisotropy*; see Figure 4.13 and note the different orientations of the true and apparent resistivity ellipses. The general rule (Wasscher, 1961) is that the resistivity measured in the direction aligned with a four-electrode linear array is the geometric mean of the resistivities in the two directions perpendicular to the electrode array.

A square electrode array, in which the current electrodes *AB* and the potential electrodes *PQ* are arranged to form a square of side *a*, often provides a greater sensitivity to anisotropy than a linear array. Boadu *et al*. (2005) acquired azimuthal resistivity data using a square array to map subsurface fractures in crystalline metamorphic rocks to support a groundwater resources assessment in an agricultural district of Ghana. Their results are shown in Figure 4.14. The polar axis shows apparent resistivity as the array is rotated about its central point. Note that the minor axis of the apparent resistivity ellipsoid aligns with the fracture direction when a square – array electrode configuration is used.

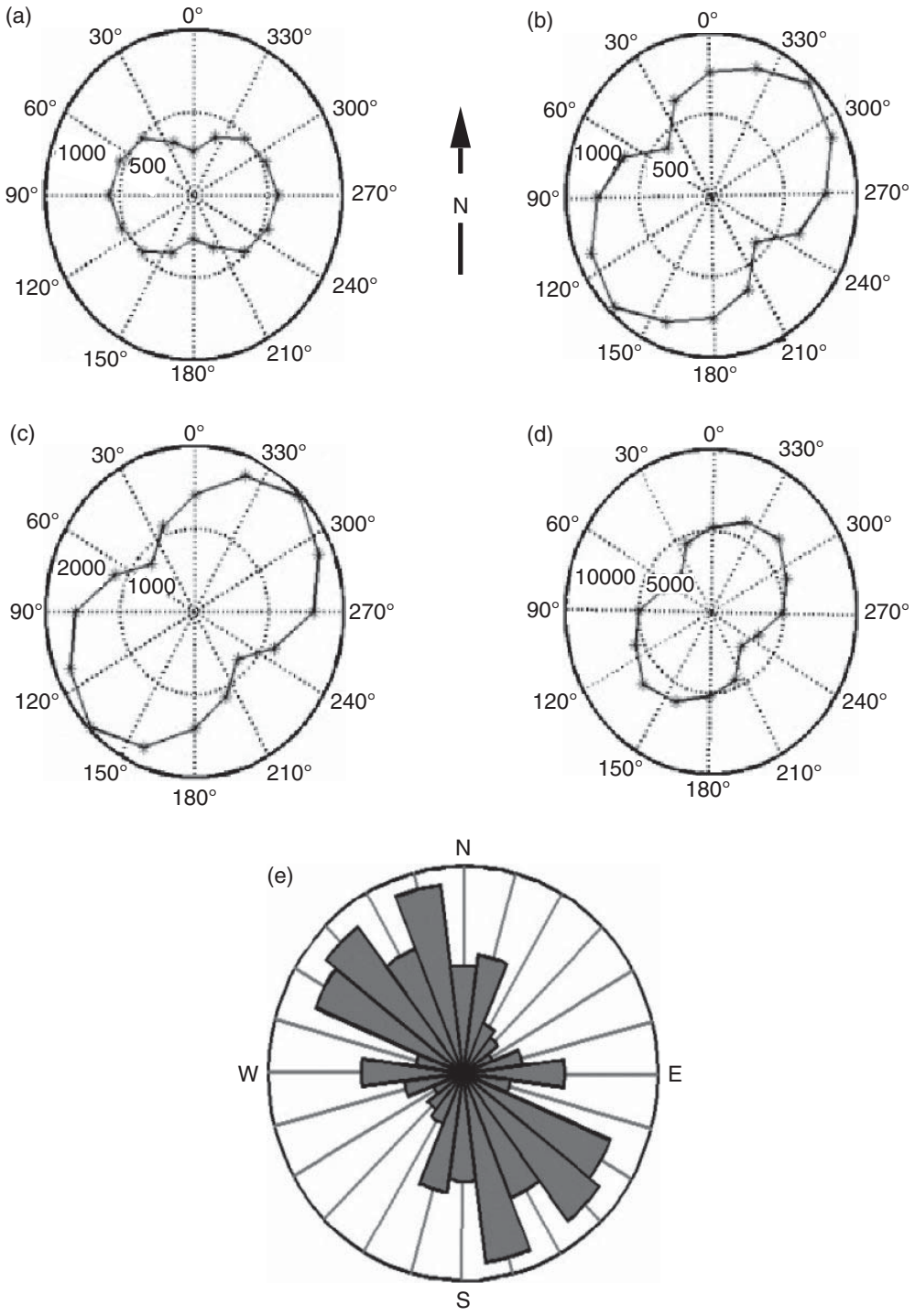

Figure 4.14 The top panels (a–d) show azimuthal resistivity ellipses from a fractured rock formation in Ghana. The bottom panel (e) shows geological fracture orientations mapped in the field. After Boadu *et al*. (2005).

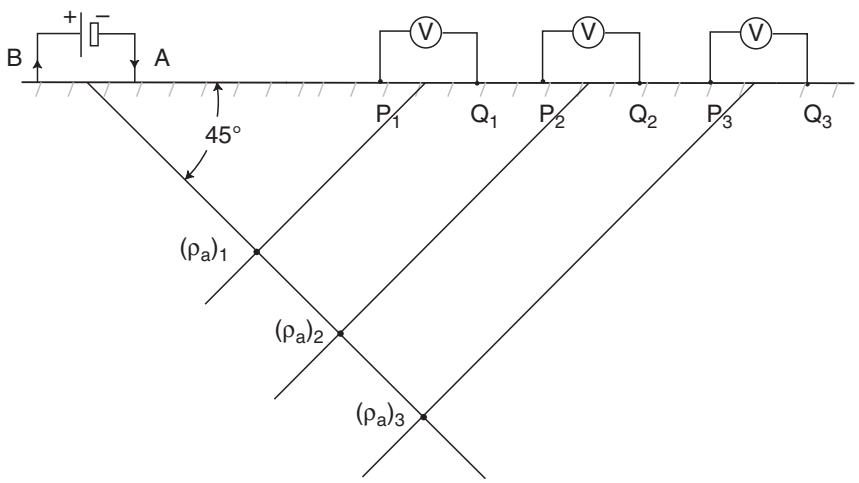

Figure 4.15 Construction of a dipole–dipole resistivity pseudosection.

4.6 Resistivity pseudosections

A convenient way to display multi-electrode resistivity data is by means of a resistivity pseudosection. As shown in Figure 4.15, the measured apparent resistivity ρ_a associated with a current AB and a potential electrode pair PQ is plotted at the intersection of two lines, each making a 45° angle with the ground surface and passing through the center of one of the electrode pairs. This procedure is repeated for each pair of current and potential electrodes. The resulting pseudosection provides a rough indication of the true Earth resistivity since the maximum sensitivity to the ground structure of a given voltage measurement occurs close to the midpoint of the four-electrode configuration at a depth of approximately one-half the separation of the current–potential electrode pairs.

To provide an example of resistivity imaging, a dataset was acquired using the multi-electrode Sting R8/IP system (www.agiusa.com), as illustrated in Figure 4.16. The acquisition protocol involved a computer-controlled sequence of Schlumberger and dipole–dipole electrode configurations, as discussed in more detail below. The observed pseudosection is shown in the top panel of Figure 4.17. The larger solid squares at the top of the pseudosection correspond to electrode locations while the smaller symbols that appear in the interior of the pseudosection mark the locations where the measured apparent resistivity is plotted. The pseudosection is displayed by contouring the apparent resistivity data. The trapezoidal shape of the pseudosection reflects the fact that the measured data are only minimally sensitive to ground structure in the two triangular regions beneath either the current or the potential electrodes.

4.7 Electrical-resistivity tomography (ERT)

Traditional electrical-resistivity soundings use a conventional electrode configuration such as Schlumberger, Wenner, dipole–dipole, pole–dipole, or pole–pole (see Figure 4.8). A sounding, in which the electrode-separation lengths are varied without moving the array

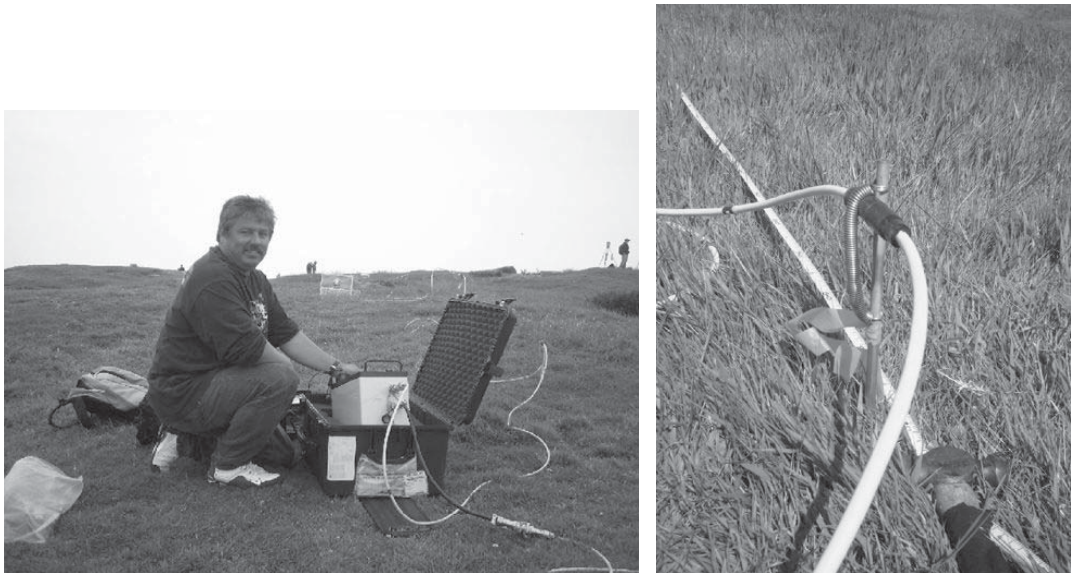

Figure 4.16 (Left) Multi-electrode resistivity system from AGI Geosciences, Inc.; (right) close-up of an electrode installation.

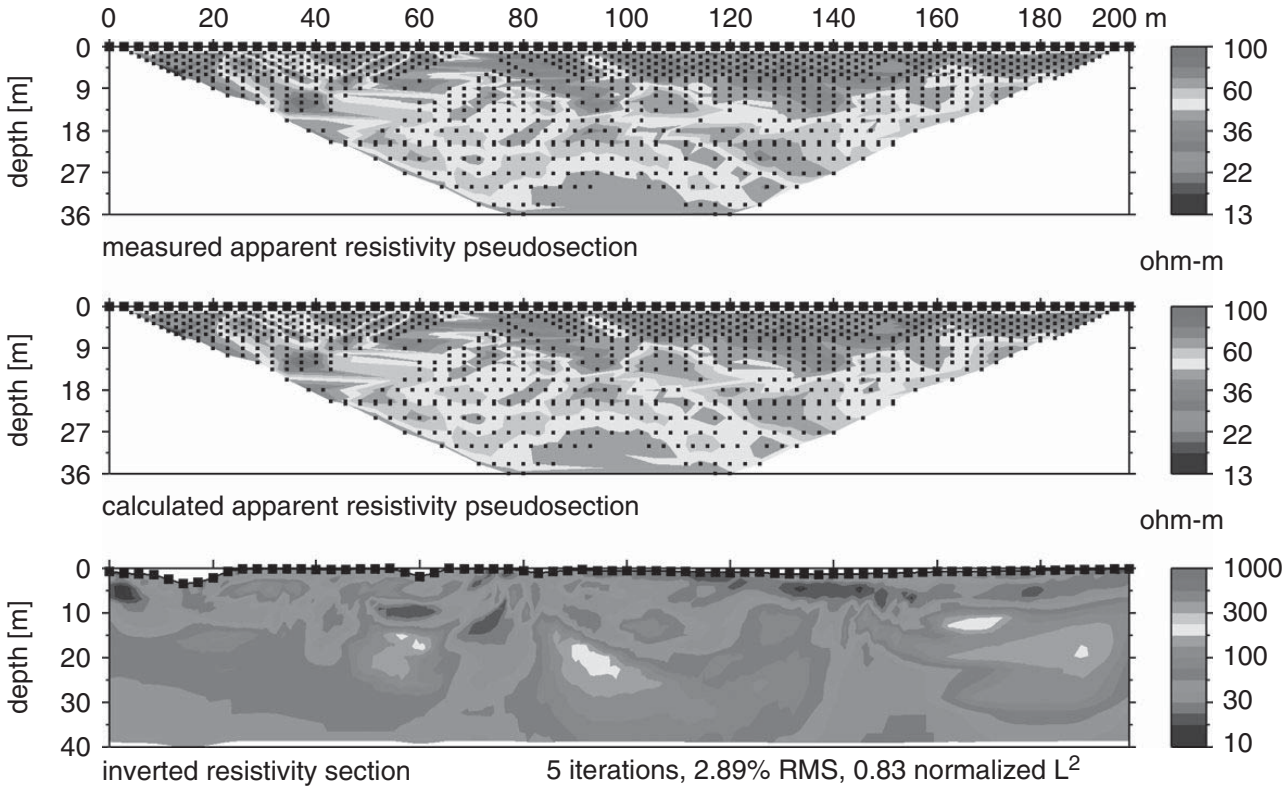

Figure 4.17 Measured apparent resistivity pseudosection (top) for a hybrid Schlumberger-DD electrode configuration, along with the inverted resistivity image (bottom). The calculated pseudosection (middle) is based on solving the forward problem for the resistivity structure shown at the bottom. Note the good match between the measured and calculated pseudosections.

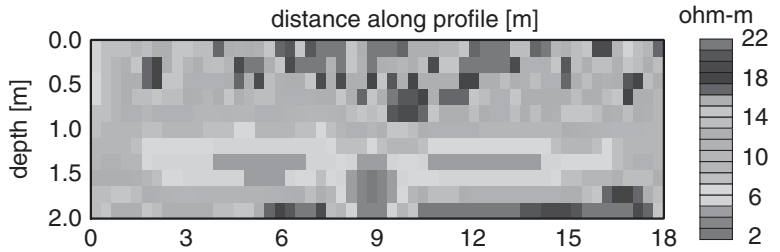

Figure 4.18 Inversion of dipole-dipole resistivity data acquired over a buried pipeline at the Texas A&M Riverside campus. The pipeline is the conductive (*red*) zone at depth 1.5–2.0 m midway along the profile. Electrode spacing is 0.3 m.

midpoint, provides a local 1-D electrical-resistivity depth model, $\rho(z)$. Alternatively, lateral profiling of $\rho(x)$ over a narrow depth interval can be achieved by traversing the electrode array along a horizontal profile without changing the electrode separations. Neither the sounding nor the profiling method alone provides an accurate indication of subsurface resistivity distribution in complex geological terrains.

Resistivity imaging of complex subsurface structures has recently advanced with the development of multi-electrode acquisition systems and 2-D and 3-D inversions. The resistivity technique for near-surface applications has surged in popularity due to these advances. Pioneering work on electrical-resistivity tomography (ERT) was published by Daily and Owen (1991) who considered a cross-borehole electrode configuration.

ERT imaging is performed by matching the measured apparent resistivity pseudosection to a computed pseudosection that is obtained by solving, for a given Earth resistivity structure $\rho(\mathbf{r})$, the governing scaled-Laplace equation $\nabla\cdot([1/\rho]\nabla\varphi) = 0$. The electric-potential distribution $\varphi(\mathbf{r})$ is evaluated at the locations of the potential electrodes and then transformed into a computed apparent resistivity. The model $\rho(\mathbf{r})$ is then adjusted, and the apparent resistivity re-computed, ideally until it matches the measured apparent resistivity to within a pre-defined acceptable tolerance. The process of forward modeling and imaging is discussed in detail in later chapters of this book. The bottom two panels of Figure 4.17 show a resistivity image and its calculated apparent resistivity response. The spatial structure of the resistivity image, in this example, reflects variations in subsurface moisture content.

A second field example of ERT imaging is shown in Figure 4.18. A dipole–dipole data set was acquired along a profile over a buried pipeline on Riverside campus at Texas A&M University. The inversion algorithm dc2dinv, which is available at www.resistivity.net, was used to construct the image. The profile uses 56 electrodes and is oriented orthogonal to the strike of the target with 0.3-m electrode spacing. The signature of the pipeline is the low-resistivity zone that appears at the midpoint of the profile, at depth ~ 2 m beneath the surface. The laterally variable structure that is evident in the upper part of the image (depths < 0.5 m) is likely caused by near-surface soil heterogeneity and irregular coupling of the electrodes to the ground.

There is a possibility for interpretation errors to occur if ERT data are aquired on a sparse set of orthogonal 2-D lines or transects and then subjected to fully 3-D modeling and inversion. Gharibi and Bentley (2005) recommend that to avoid artifacts the line spacing

should be not more than two–four times the electrode spacing. Measurements should be made, if possible, using a wide range of azimuths of the line joining the midpoints of the current–electrode pair and the potemtial–electrode pair. Furthermore, the electrode spacing should not be greater than the dimensions of the smallest feature to be imaged.

4.8 Electrical properties of rocks

In the shallow subsurface, the most important geological factor that controls the bulk electrical resistivity is the spatial distribution of pore-fluid electrolytes. The aqueous pore fluids may be contained in pores, fractures, or faults. Electrical geophysical investigations have been used in various hydrogeological, environmental, geotechnical, and civil-engineering applications.

A fundamental assumption of the electrical and electromagnetic methods of geophysics, including the electrical-resistivity technique, electromagnetics (EM), and ground-penetrating radar (GPR), is that the underlying geological medium is electrically neutral, containing vast but equal numbers of positive and negative charge carriers. Some of the charges are free or quasi-free to migrate, or drift, from place to place within the geological medium. Other charges are bound to lattice atoms or other microscopic, localized "charge centers" (Jonscher, 1977), or they are held at material interfaces. Bound charges play no role in the electrical-resistivity or EM techniques but as the reader will see in later chapters they are significant in shaping GPR, induced polarisation (IP), and self-potential signals. Electrical conductivity σ measures the capability of a material to sustain long-term current flow via the charge migration mechanism. By longstanding convention, the electrical resistivity $\rho = 1/\sigma$ is the material parameter used to interpret data acquired using the electrical-resistivity technique but herein we use conductivity and resistivity interchageably. Two significant types of charge polarization, atomic and molecular, and two types of charge migration, semi-conduction and electrolytic conduction, are illustrated in Figure 4.19.

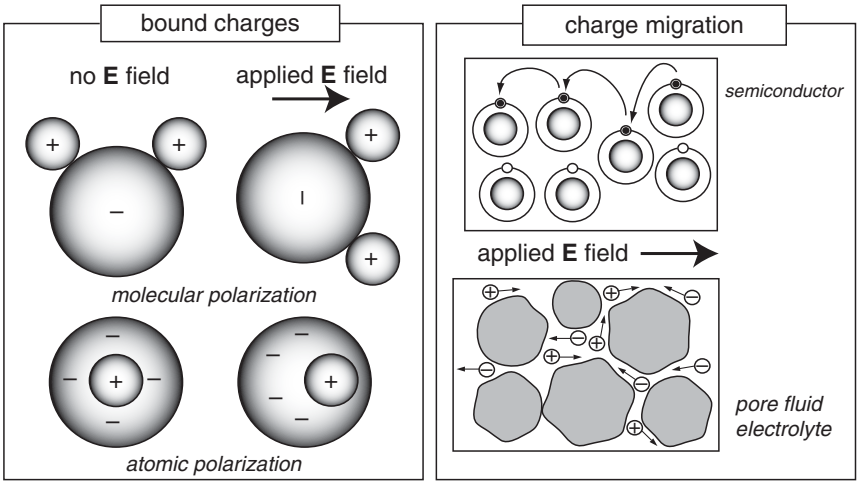

Figure 4.19 Electrical-polarization (left) and -migration (right) mechanisms.

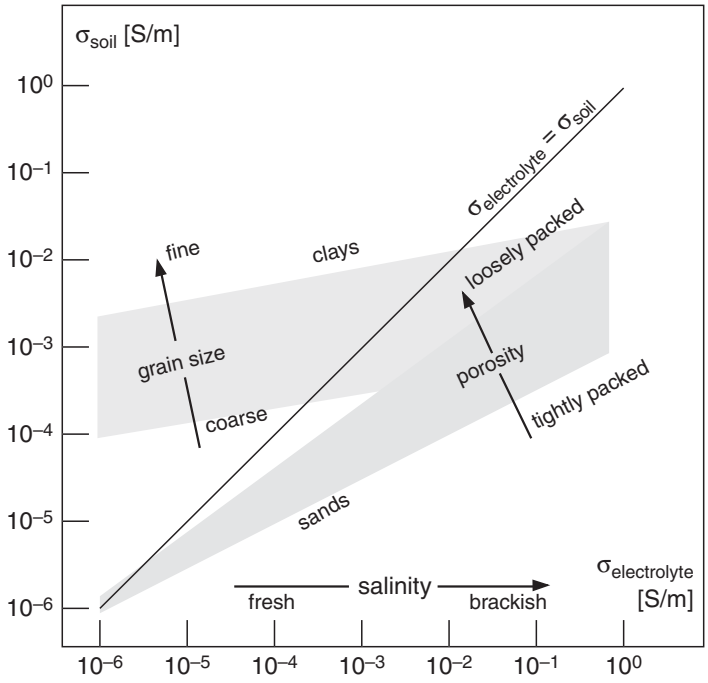

Figure 4.20 Electrical conductivity of saturated soils, after Santamarina *et al*. (2005).

Electrical conduction in most rocks is *electrolytic*, with ions in the pore fluids being the predominant charge carriers. The solid matrix of grains is typically semi-conducting, with notable exceptions being metallic grains and the surface of certain clay minerals, which are conducting. The pore space in a rock is generally much more conductive than the solid grains owing to the presence of dissolved ions in the pore-fluid solution.

Electrolytic conductivity increases, or equivalently, resistivity decreases with increasing salinity, porosity ϕ, and temperature T. A high-salinity pore fluid has a greater concentration of ions available for conduction; a rock with high interconnected porosity often has an abundance of paths for conduction; higher temperature enhances the mobility of ions. The variation of bulk electrical conductivity as a function of salinity, for sand-dominated and clay-dominated saturated soils, is outlined in Figure 4.20.

Purely siliciclastic rock units such as clean, unfractured sandstones typically exhibit a fairly regular intergranular, or primary, porosity that developed as the original sediment compacted and lithified. The pore space in such rocks usually forms an interconnected network with open intergranular spaces that are connected by clear throats. A well-sorted sandstone of this type has a high permeability.

In clean, unfractured sandstones characterized by water saturation S_W and porosity ϕ, the traditional Archie's law (Archie, 1942) gives the bulk electrical conductivity σ [siemens per meter, S/m] as

$$\sigma = a\sigma_W S_W^n \phi^m. \tag{4.37}$$

This empirically based relationship with saturation exponent $n \sim 2$ has long been used by petroleum geoscientists and more recently by hydrogeophysicists to describe the bulk

electrical conductivity σ of hydrocarbon reservoirs and aquifers. The parameter m, historically known as the cementation exponent, depends on the grain shape and generally lies within the range $m \sim 1.2$–2.2 for sandstones (Worthington, 1993). The leading coefficient a can vary widely depending on the pore cementation, tortuosity, grain size and shape, fluid wettability, clay content, and numerous other factors.

The quantity $\sigma_W \sim 0.3$–1.0 S/m (Keller and Frischknecht, 1966) in Equation (4.37) is the electrical conductivity of the pore electrolyte, which is controlled by the salinity, or more generally the total dissolved solids in the pore water. Commonly, an intrinsic formation factor $F = \sigma_W/\sigma$ for a fully water-saturated ($S_W = 1$) rock unit is defined. Since pore fluids are electrically conductive relative to the solid rock matrix, we have $\sigma_W > \sigma$ and hence $F > 1$. From Archie's law (4.37), for a fully saturated rock we see that the formation factor is related to porosity by $F \sim \phi^{-m}$.

Clay minerals originating from secondary diagenetic processes can coat the sand grains and clog the pore throats, reducing the porosity and permeability. A general rule of thumb is that high-porosity sandstones are likely to be clean while low-porosity sandstones are likely to be shaly. Clay minerals also have an inherent negative surface charge which contributes an additional electrical conduction pathway that is not found in clean sandstones. Thus, clay-bearing formations generally have a considerably higher bulk electrical conductivity than clean sandstones.

Waxman and Smits (1968), Worthington (1993), and others have demonstrated that important modifications to Archie's formula are necessary in the case of shaliness. These studies suggest that the intrinsic formation factor $F = \sigma_W/\sigma$ should be regarded only as an *apparent* formation factor F_a and that shale effects might be responsible for much of the observed variability in the Archie parameters (a, m). The shale effect on the formation factor is described by the Waxman–Smits equation

$$F_a = F\left[1 + \frac{\tilde{\sigma}}{\sigma}\right]^{-1} = \frac{\sigma_W}{\sigma + \tilde{\sigma}}, \tag{4.38}$$

where $\tilde{\sigma}$ is the "excess conductivity" of the rock that accounts for the surface conduction associated with the clay particles, including the effects of the cation-exchange reactions that occur between the clay and the saturating electrolye. Numerical values for $\tilde{\sigma}$ can be computed from basic electrochemical tables if the composition and concentration of the saturating electrolyte is known. When shale effects are absent, $\tilde{\sigma} \to 0$ and $F_a \to F$ in Equation (4.38), as expected.

Geological interpretation of resistivity data is more problematic in carbonate terrains than in sands. Carbonate rock units commonly exhibit secondary porosity, such as moldic vugs caused by anhydrite dissolution of fossil remains, that develop after the rock is formed. The secondary porosity can carry a considerable fraction of the permeability. The bulk permeability depends strongly on whether the vugs are separate or touching each other (Lucia, 1983). It is very difficult to make an assessment from studying outcrops and drilled core samples about the role of vugs in shaping the bulk hydrogeological behavior of a carbonate formation. Furthermore, the range of intergranular textures found in carbonate rocks varies greatly from coarser grain-dominated to finer mud-dominated fabrics.

In carbonates, the relationship between electrical resistivity and porosity is quite complicated (Summers, 2006). Archie's law has limited predictive value in carbonates as the m value can vary widely and it is difficult to ascertain for a given formation. Cementation exponent values as high as $m \sim 4$–7 have been observed in Middle East oil reservoirs. Asquith (1995) has noted that large values of m are associated with higher separate-vug porosities, while a lower m value is associated with touching-vug porosity, such as fractures.

4.9 Electrical–hydraulic field-scale correlation studies

A long-standing debate amongst near-surface geophysicists has arisen about whether it might be possible to interpret geoelectrical measurements in terms of aquifer bulk properties. Resolution of this issue is one of the main focus points of the rapidly expanding field of hydrogeophysics (Slater, 2007). The capability to convert electrical geophysical data into estimates of bulk aquifer properties such as transmissivity or storativity, for example, would represent a major breakthrough in the field of water-resources research.

Many laboratory studies over the past several decades have claimed to discover links between electrical and hydraulic properties of rock samples. Early investigations by Katz and Thompson (1986), for example, received a great deal of attention. They proposed a relationship of the form

$$k \sim \frac{l_c^2}{226}\left(\frac{\sigma}{\sigma_W}\right), \tag{4.39}$$

where k [darcies, D = μm^2] is the fluid permeability, l_c [μm] is a characteristic length of the pore space, and σ is the electrical conductivity of a rock sample saturated with a brine solution of electrical conductivity σ_W. Katz and Thompson (1986) explain how l_c is determined in the laboratory from mercury-injection experiments.

Equation (4.39) suggests that a positive correlation exists between the fluid-transport property k and electrical conductivity. Huntley (1986) has shown however that the electrical–hydraulic (σ, k) relation in rock samples can also be negatively correlated. The latter case is readily understood in clay-bearing samples where the presence of clay increases the bulk electrical conductivity, due to enhanced surface conduction effects, but at the same time decreases the bulk fluid permeability since clay particles generally clog the pores. A good discussion of the complexities involved in establishing petrophysical relationships between electrical and hydraulic properties, at the sample scale, is provided by Lesmes and Friedman (2005).

While laboratory experiments can provide a fundamental basis for understanding electric–hydraulic correlations at the sample length scale (~ 0.1–10 cm), of greater interest here are linkages at much larger field scales (~ 10 m–1 km) between geoelectrical measurements and aquifer properties.

A simple interpretive rule, which strictly applies only under ideal geological conditions, has been suggested by MacDonald *et al*. (1999). Consider a clean, sandy aquifer. Standard hydrological theory predicts, in this case, a direct relation between porosity ϕ and hydraulic conductivity K. Furthermore, based on Archie's law (4.37), an inverse relation is expected between porosity ϕ and resistivity σ, where σ is the reciprocal of conductivity σ. Thus, in idealized clay-free aquifers the product $K\sigma$ is approximately constant. On the other hand, it is well known that in clay-rich aquifers the hydraulic conductivity and electrical resistivity are both controlled by the clay content rather than the porosity. Since K and σ both increase in direct relation to the clay content, to first order, we have that the quotient K/σ should remain roughly constant in ideal clay-rich aquifers.

MacDonald *et al*. (1999) rely on the foregoing analysis to relate a bulk aquifer property to the bulk electrical resistivity inferred from surface-based electrical geophysical measurements. Consider the aquifer transmissivity $T = Kh$, where h is the aquifer thickness. Suppose also that a 1-D-layered resistivity sounding curve has been acquired over the aquifer. Such a curve could be constructed, for example, from an inversion of Schlumberger or dipole–dipole apparent-resistivity measurements. If the resistivity of the layer that corresponds to the aquifer is comparatively high, the aquifer is likely to have a low clay content and it can be shown that the best-resolved geoelectrical parameter is the transverse resistance $R_t = h\sigma$ of the layer. Similarly, the longitudinal conductance $L_c = h/\sigma$ is the best-resolved parameter in the case of a clay-rich, comparatively conductive layer.

For the clay-free aquifer, we can combine the finding that $K\sigma$ is constant with the definitions $R_t = h\sigma$ and $T = Kh$ to deduce that

$$T = C_1 R_t. \tag{4.40}$$

In other words, the aquifer transmissivity is in direct proportion to the geophysically determined transverse resistance of the aquifer. Similarly, for the clay-rich aquifer it follows that

$$T = C_2 L_C, \tag{4.41}$$

or the transmissivity is in direct proportion to the longitudinal conductance. The appropriate constant C_1 or C_2 can be determined by comparing the resistivity sounding curve to hydraulic data at locations where the transmissivity has been determined by pump tests. Then, using geophysics and either Equation (4.40) or (4.41) depending on the aquifer type, an estimate of the aquifer transmissivity can be extrapolated to areas outside the region of influence of the available pump tests. This is a valuable exercise since pump tests are much more expensive to carry out than surface geophysical measurements. MacDonald *et al*. (1999) have used this method to estimate the spatial distribution of transmissivity of the gravel aquifer at Desborough Island on the Thames River near London. The result is shown in Figure 4.21.

A different approach for interpreting geoelectrical measurements in terms of aquifer properties was suggested by Soupios *et al*. (2007) who combined information from wells with 1-D inversions of Schlumberger vertical electric sounding data acquired at a number

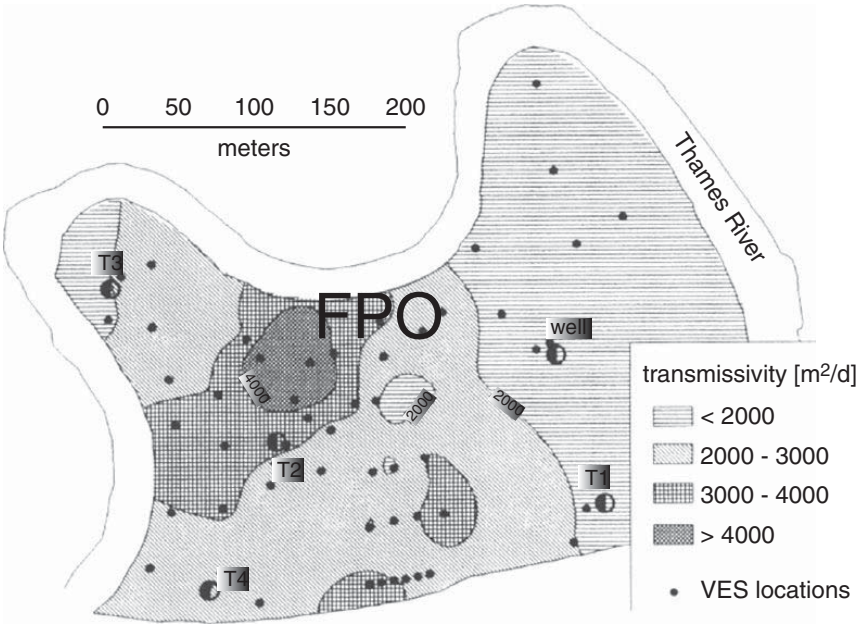

Figure 4.21 Transmissivity of the subsurface gravel aquifer at Desborough Island, UK. Point estimates are obtained from pump tests at locations T1–T4. Spatially distributed estimates are obtained from ~ 50 electrical geophysical soundings (VES), marked by the small black dots. After MacDonald *et al*. (1999).

of sites on the island of Crete. The conversion from resistivity to hydraulic conductivity was performed using the geophysically inferred value of the porosity ϕ, as follows. In the clay-bearing aquifer at Crete, Archie's law (4.37) no longer applies and consequently the Waxman–Smits equation was used. Re-arranging Equation (4.38) gives

$$\frac{1}{F_a} = \frac{1}{F} + \tilde{\sigma}\,\rho_W, \tag{4.42}$$

such that a plot of the inverse of the apparent formation factor F_a against the pore-fluid resistivity σ_W yields an intercept of $1/F$. The apparent formation factor F_a at each sounding location on Crete was evaluated using bulk resistivity σ from inversion of the Schlumberger data along with the fluid resistivity σ_W measured from a nearby well. The intrinsic formation factor F was obtained from a linear regression based on Equation (4.42), and then converted into porosity ϕ using Archie's law. Then the hydraulic conductivity k [m/day] of the aquifer was computed using the standard hydrology equation (Domenico and Schwartz, 1990)

$$k = \frac{480\delta_W g d^2 \phi^3}{\mu(1-\phi)^2}, \tag{4.43}$$

where d [m] is the grain size, $g = 9.80$ m/s^2 is gravity, $\delta_W = 1000$ kg/m^3 is the fluid density, and $\mu = 0.0014$ kg/m s is the fluid dynamic viscosity. Finally, the aquifer transmissivity $T = kh$ [m^2/d] was evaluated using Equation (4.43) along with the known thickness of the aquifer obtained from the nearby wells. The resulting spatial distribution of aquifer transmissivity is shown in Figure 4.22.

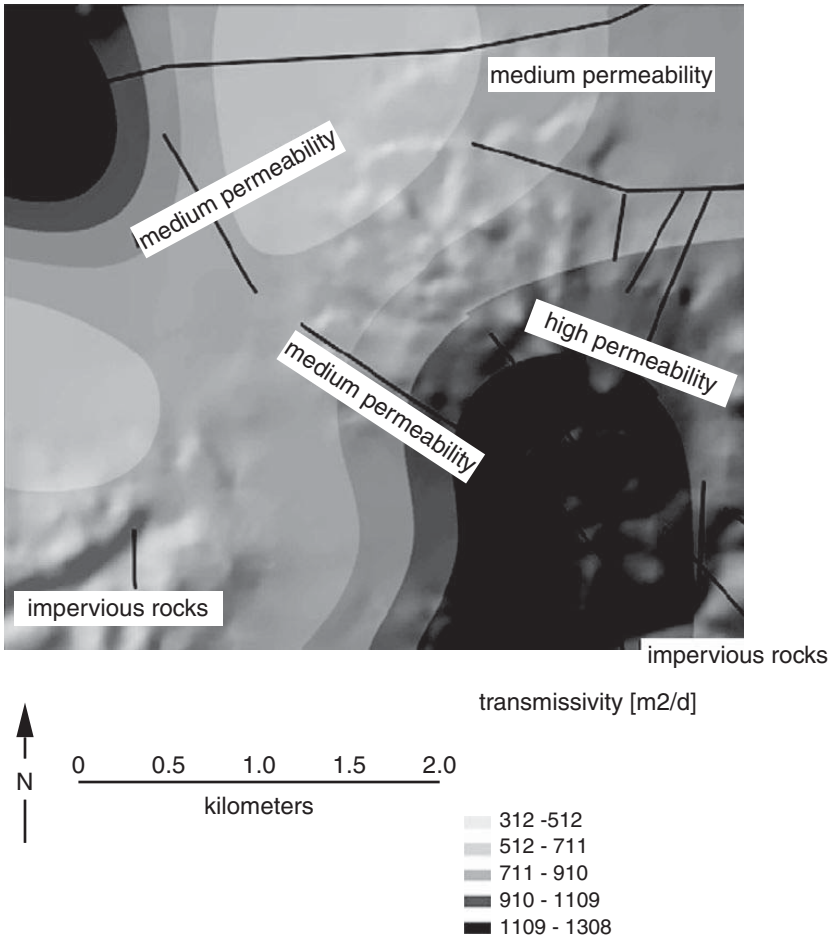

Figure 4.22 Transmissivity of the Keratis basin aquifer in Crete based on Schlumberger electrical soundings. After Soupios *et al*. (2007).

4.10 Optimal electrode placement

Extensive field tests and sensitivity studies have indicated that each of the traditional electrode configurations has strengths and weaknesses. With the advent of computer-controlled multi-electrode acquisition capabilities (e.g. Loke, 2000), data can be recorded using a variety of standard and non-standard configurations. The combined dataset can then be inverted to obtain a 2-D or 3-D subsurface model.

Consider a linear array of d equally spaced electrodes. There are a total of

$$D = d(d-1)(d-2)(d-3)/8 \tag{4.44}$$

possible four-point (one current source, one current sink, and two potential measurement) electrode configurations. For example, if $d = 50$ electrodes are laid out, this leads to $D =$ 690 000 possible four-point measurements, each of which takes $\sim$ 1 s to acquire.

Commercial systems routinely use $d > 100$ electrodes. Thus, acquisition of a *comprehensive dataset* of D responses is impractical.

It is of interest, therefore, to determine whether limited combinations of electrode configurations can supply subsurface resistivity images that are comparable in quality to images that would be generated from a comprehensive dataset. An experimental design procedure has been developed by Stummer *et al*. (2004) to achieve this goal. A non-linear objective function is defined and maximized using a global optimization technique.

The performance of traditional electrode configurations is evaluated using a synthetic model (Figure 4.23a, left panel) consisting of a thin, moderately conductive ($\rho = 100$ Ωm, typical of silt) near-surface layer overlying a resistive ($\rho = 1000$ Ωm, typical of dry gravel) basement. A highly conductive ($\rho = 10$ Ωm) block and a highly resistive ($\rho = 10\,000$ Ωm) block are embedded in the model to provide lateral heterogeneity, as shown.

A simulated resistivity configuration using $d = 30$ (such that $D = 82\,215$) electrodes with spacing $\Delta x = 5$ m is deployed along the top of the model. Omitting certain combinations that yield intrinsic poor data quality, such as crossed-dipole and very-long-offset dipole–dipole configurations, a simulated data set of size $D = 51\,373$ is generated using a standard finite-difference modeling code. The synthetic data $\mathbf{d}_{OBS}$, consisting of logarithmic voltage readings, are then inverted (see Chapters 11–13) using an iterative scheme

$$\mathbf{m}_{i+1} = \mathbf{m}_i + G^{-g}(\mathbf{d}_{OBS} - \mathbf{d}[\mathbf{m}_i]) \tag{4.45}$$

where $\mathbf{m}_i$ is a vector of parameters which describe the resistivity model, and $\mathbf{d}[\mathbf{m}_i]$ is the computed data based on model $\mathbf{m}_i$.

The quantity $G^{-g} = (G^T G + C_M^{-1})^{-1} G^T$ is the generalized stable inverse of the Jacobian matrix $\mathbf{G}$ defined by

$$G_{ij} = \frac{\partial ln V_i}{\partial ln \rho_j}, \tag{4.46}$$

and $\mathbf{C}_M$ is the model covariance matrix, which includes damping or smoothing constraints on the model parameters. In Equation (4.46), ρ_j is the electrical resistivity of the j-th model cell of the total of P cells. Thus, the dimension of matrix G is $D \times P$. Inversion results for the synthetic test model are shown in Figure 4.23b–e, left panel. Note that the best model recovery is associated with the comprehensive data set. The conductive body at the left is not seen using the Wenner and/or dipole–dipole data sets.

In the experimental design procedure of Stummer *et al*. (2004), a homogeneous half-space of uniform resistivity is used as a starting model. Assume an initial data set of size $D_0 << D$, based on a traditional array such as dipole–dipole. The key design step is to determine which additional electrode configurations would provide the most new information about the subsurface. A quantitative measure of information is provided by the Jacobian sensitivity matrix.

Suppose that the 2-D resistivity model consists of $P = pq$ cells. The Jacobian of the comprehensive dataset is denoted by G^C. The Jacobian of the initial data set is G^0. The two Jacobians have dimensions $dim G^C = D \times pq$ and $dim G^0 = D_0 \times pq$, respectively. We can define a new $(D - D_0) \times pq$ matrix G^1 according to $G^C = [G^0 | G^1]$, which corresponds to

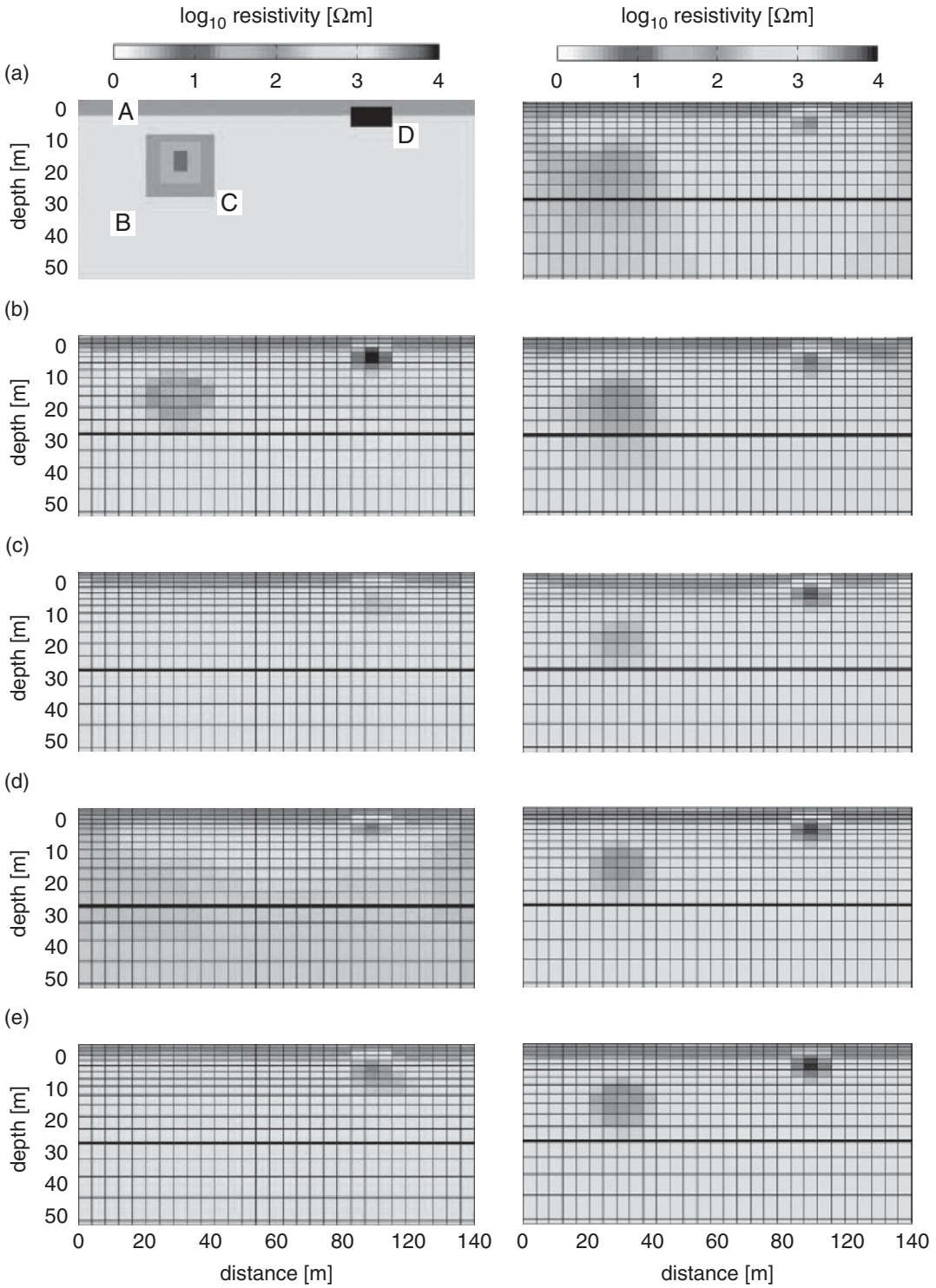

Figure 4.23 (Left panel) Resistivity inversion test, after Stummer *et al*. (2004), (a) starting model. Inversion results using: (b) comprehensive dataset, $D = 51\,373$; (c) Wenner $D = 135$; (d) dipole–dipole $D = 147$; (e) Wenner/dipole–dipole $D = 282$ electrode configurations. (Right panel) Resistivity inversion based on optimal experimental design, after Stummer *et al*. (2004), (a) $D = 282$; (b) $D = 670$; (c) $D = 1050$; (d) $D = 5740$; (e) $D = 10\,310$ electrode configurations.

the remaining, unacquired dataset. We can also define the resolution matrices $R^C = (G^C)^{-g} G^C$ and $R^0 = (G^0)^{-g} G^0$. The i-th electrode configuration in the unacquired dataset is considered to provide important information if it generates a large value of the *goodness function* $\Psi(i)$, where

$$\Psi(i) = \sum_{j=1}^{pq} \frac{|G_{ij}^1|}{G_j} \left[1 - \frac{R_{jj}^0}{R_{jj}^C} \right]. \tag{4.47}$$

The normalization factor

$$G_j = \frac{1}{D} \sum_{i=1}^{d} |G_{ij}^C| \tag{4.48}$$

compensates for the natural tendency of near-surface cells to dominate the sensitivity calculation. Note that $\Psi(i)$ is large when the elements of the corresponding row of matrix G^1 are large. Since a diagonal element $R_{jj} = 1$ indicates a perfect resolution of the j-th model parameter, the term $1 - R_{jj}^0 / R_{jj}^C$ appearing in Equation (4.47) forces the goodness function $\Psi(i)$ to favor electrode configurations that can constrain unresolved model parameters.

The goodness function $\Psi(i)$ in Equation (4.47) is only one of many that could be usefully defined in an optimal experimental design. We can rank the electrode configurations in the unacquired dataset according to their values of the goodness function. The ones that generate the highest goodness function are then used to generate the next dataset. An electrode configuration is rejected if it is linearly independent (as determined by their respective rows in the comprehensive Jacobian matrix) to a configuration used in the initial dataset. An example of optimized inversion using the synthetic example is shown in Figure 4.23, right panel.

4.11 Underwater resistivity techniques

A review of developments in marine electrical and electromagnetic geophysical techniques, including resistivity, IP, and EM methods, is provided by Butler (2009). A summary of the literature shows that there has developed in recent years two common modes of operation for underwater resistivity surveys. In a mode of operation (Day–Lewis *et al.*, 2006; Passaro, 2010) that is particularly suited for a number of shallow-water applications including mapping coastal freshwater discharge and nautical archaeology, an array of floating electrodes is towed on the water surface behind a vessel (Figure 4.24). Such systems can achieve continuous resistivity profiling of the subbottom resistivity structure and have detected seabed anomalies caused by shipwrecks. Other studies have attempted to use bottom-towed electrode arrays but these can be easily damaged as they are dragged across the rugged seafloor.

In another mode of operation, the electrode array is stationary. In some cases an array of grounded electrodes is employed that makes direct electrical contact with the subbottom, as in conventional land surveys. In deeper water, electrodes may be suspended on vertical cables extending from buoys or a vessel at the sea surface into the water column. This approach was used by Baumgartner and Christensen (1998). The choice of which marine

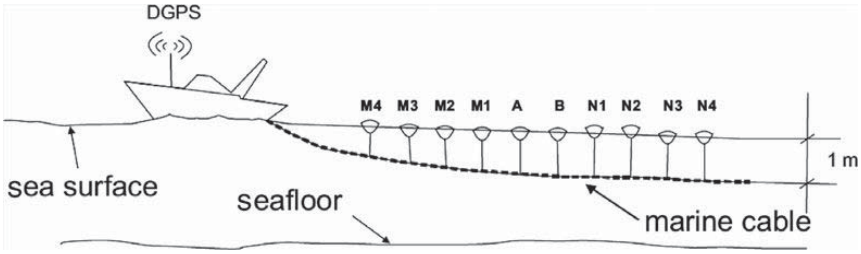

Figure 4.24 A surface-towed electrode array for marine resistivity surveys. DGPS = differential GPS navigation system. After Passaro (2010).

resistivity survey geometry to adopt for a particular project should be dictated by forward modeling of the sensitivity of the apparent resistivity pseudosection to perturbations in the expected geological scenarios, as well as logistical and budget constraints.

4.12 Illustrative case histories

Example. Tunnel construction in the Alps.

Geophysical investigations using the resistivity method were carried out in the Col di Tenda region of the Alps near the Italy–France border where the construction of a new highway tunnel is planned. Better information on the subsurface geology is required in order to determine accurate geotechnical rock-mass quality parameters so that the safety of the excavation and long-term integrity of the finished structure is ensured. A resistivity section oriented perpendicular to the planned tunnel route is shown in Figure 4.25a. Electrode spacing is 12.0 m and depth of penetration is ~ 200–300 m.

The interpretation of the resistivity section (Figure 4.25b) is based on geological outcrop and stratigraphy from boreholes. High-angle normal faults, pervasive in this region, cause the sharp lateral resistivity contrasts seen in the geoelectric section. The low-resistivity zone at the base of the fault-bounded central graben is caused by fluid circulation within an intensely fractured Jurassic limestone layer which underlies higher-resistivity Eocene calcarenites. These resistivity and complementary seismic data were able to provide detailed structual and geological information to assist the planning of this major civil-engineering project.

Example. Brownfield redevelopment.

Many urban areas contain abandoned sites that are legacies from past industrial activities. These sites often contain hazardous materials, such as polycyclic aromatic hydrocarbons and heavy metals, in addition to rubble, metal scraps, old building foundations, and other construction debris. Often it is desired to rehabilitate these sites for re-use such as commercial or residential redevelopment. Boudreault *et al*. (2010) have described geophysical work performed at such a site in downtown Montreal, Canada (Figure 4.26a)

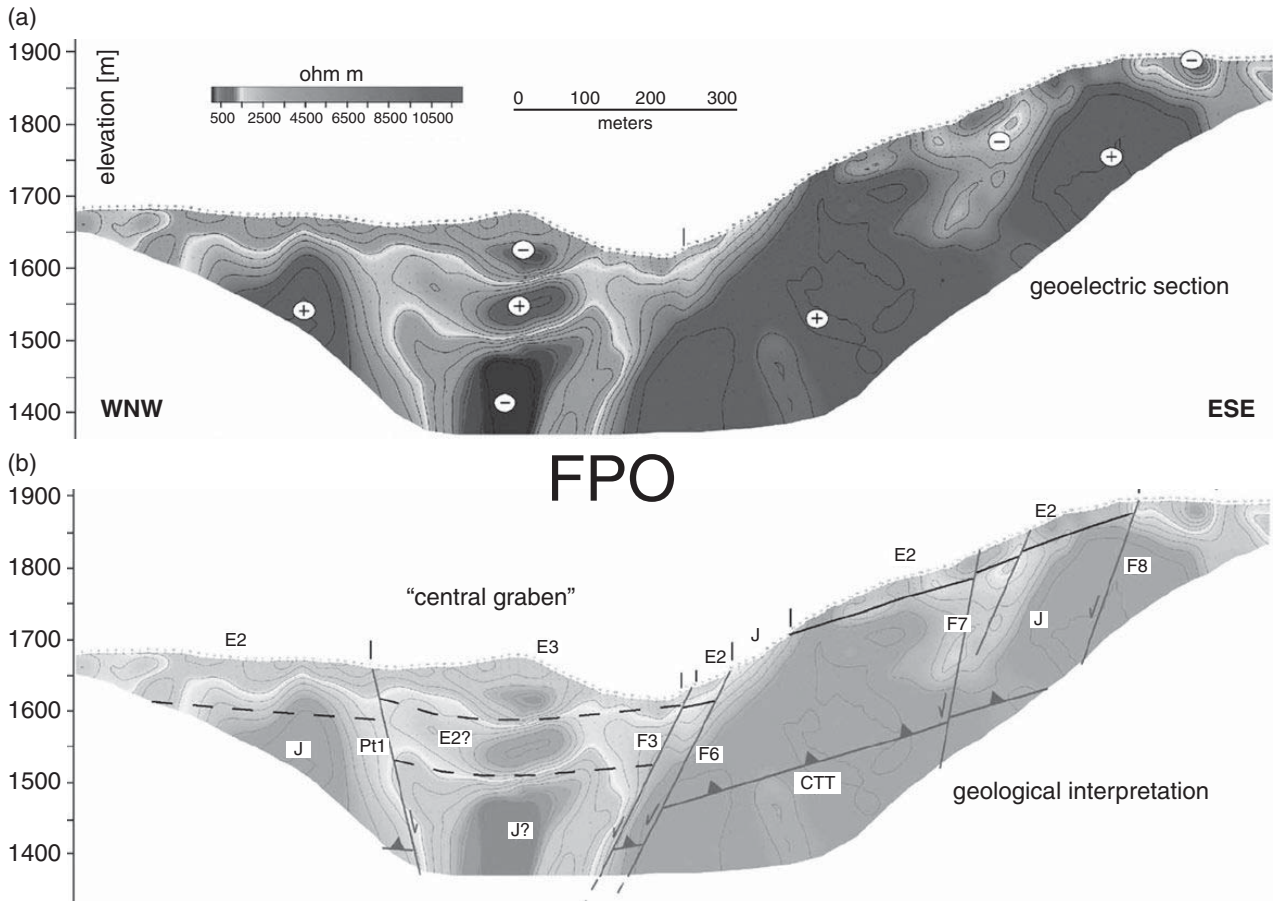

Figure 4.25 (a) Resistivity section for design of tunnel construction in Italian Alps. (b) Geological interpretation. J = Jurassic formation; E,F = Eocene formations. After Cavinato *et al*. (2006).

where new commercial development is reclaiming a long-disused parcel of urban real estate. The site is characterized by abundant heterogeneous urban fill (Figure 4.26b) that trench excavations have shown to occupy the upper ~ 2 m beneath the surface. A total of six ERT profiles were acquired, two of which are indicated in Figures 4.26c, d. The ERT images show that the upper fill layer is of higher resistivity than the underlying low-resistivity layer of natural soil. The upper layer is also strongly heterogeneous reflecting the unorganized spatial distribution of the constituent concrete and brick debris. The upper layer is more resistive than the underlying natural soil since construction materials such as brick and soil are inherently resistive (up to 1000 Ωm) compared to the natural soil and, furthermore, the upper layer is less compacted than the underlying soil and therefore has a much smaller water retention capacity, raising its resistivity. This case study shows that electrical geophysics can play a significant role in the detailed subsurface characterization of brownfield sites. The information obtained using geophysics can be used for a number of purposes, for example, it enables better assessments of potential pollutant distributions and it can help to guide the safe excavation of the site as it undergoes redevelopment.

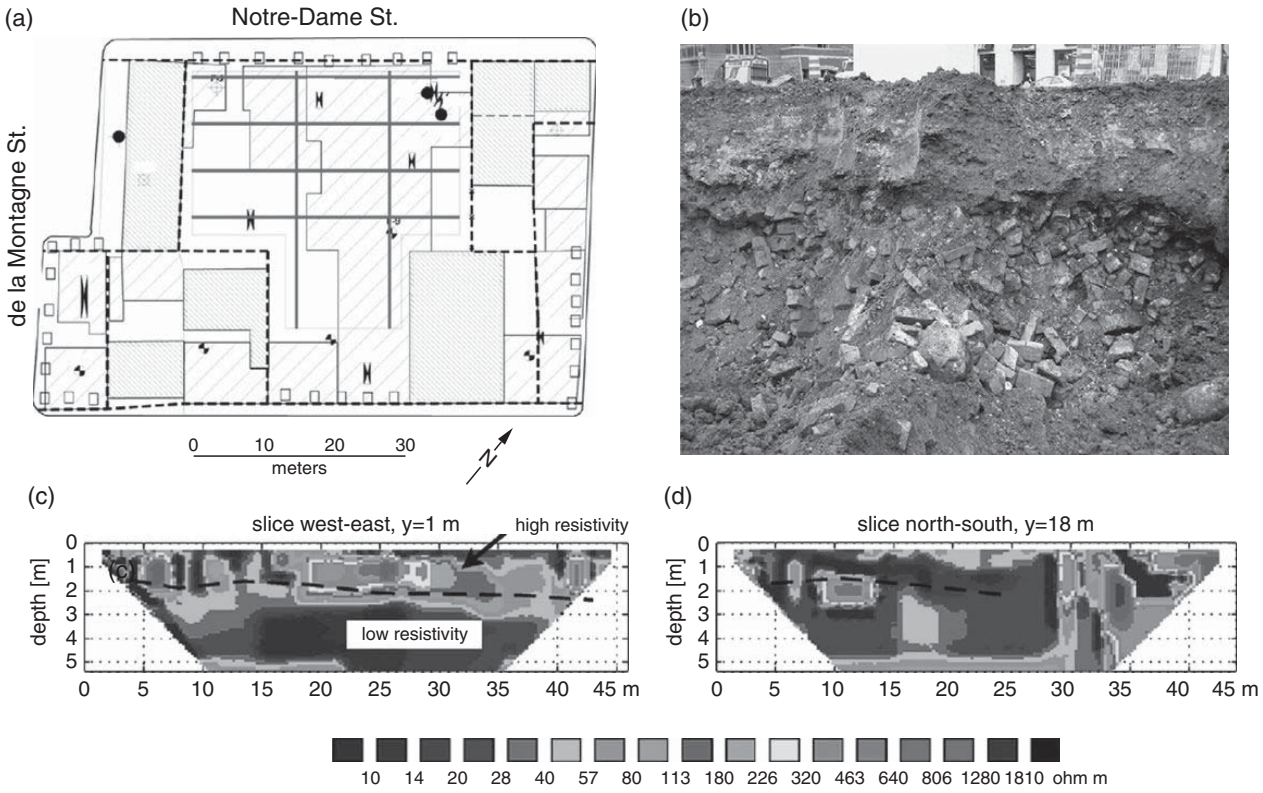

Figure 4.26 (a) Map view of urban redevelopment site, downtown Montreal, Canada. The red lines show ERT profiles. (b) Heterogeneous urban fill containing bricks, concrete, and metal debris. (c) an east–west ERT profile. (d) a north–south ERT profile. The dashed line shows the boundary between the heterogeneous fill and the natural soil, as determined by trench excavations. After Boudreault *et al*. (2010).

Problems

1. Show that the geometric factor κ for the arbitrary four-electrode arrangement is given by $\kappa = 2\pi\,[1/r_{AP}–1/r_{AQ}–1/r_{BP} + 1/r_{BQ}]^{-1}$.
2. Derive the geometric factors κ for the traditional four-electrode Schlumberger, Wenner, and dipole–dipole configurations.
3. Derive the geometric factor κ for a square array, in which the two current electrodes AB and the two potential electrodes PQ form a square of side a. Consider both cases: (i) the current electrodes are adjacent to each other; and (ii) they are diagonally opposite to each other (the *cross-square array*). Is the result of case (ii) surprising?
4. Consider a pole–pole resistivity experiment over a set of vertical fractures which can be considered as a uniform anisotropic halfspace. The potential at distance r from a point source of current I is given by

$$V(r) = \frac{I\rho_m}{2\pi r}[1 + (\lambda^2 - 1)\sin^2\varphi]^{-1/2}$$